Neurobiology of Disease 199 (2024) 106594

Contents lists available at ScienceDirect

Neurobiology of Disease

journal homepage: www.elsevier.com/locate/ynbdi

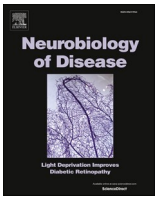

Patient-specific mutation of *Dync1h1* in mice causes brain and behavioral deficits

Raddy L. Ramos [a,*], Maider Michelena Beltran De Heredia [b,1], Yongwei Zhang [c], Randy F. Stout [d], Jaafar O. Tindi [e], Liching Wu [f], Gary J. Schwartz [g], Yair M. Botbol [h], Simone Sidoli [i], Ankita Poojari [j], Tammy Rakowski-Anderson [k], Bridget Shafit-Zagardo [l,*]

[a] *Department of Biomedical Sciences, New York Institute of Technology, College of Osteopathic Medicine, Riland Academic Health Center, Room 26, Old Westbury, NY 11568, United States of America*
[b] *BS Biotechnology, Francisco de Vitoria University, Madrid, Spain*
[c] *Cancer Center, Albert Einstein College of Medicine, 1301 Morris Park Ave, Price Building, Rm 269, Bronx, NY 10461, United States of America*
[d] *Department of Biomedical Sciences, New York Institute of Technology, College of Osteopathic Medicine, Riland Academic Health Center, Room 22, Old Westbury, NY 11568, United States of America*
[e] *Dominick P. Purpura Department of Neuroscience, Albert Einstein College of Medicine, Kennedy Center, Rm 501, 1410 Pelham Parkway S., Bronx, NY 10461, United States of America*
[f] *Dept of Medicine, Albert Einstein College of Medicine, United States of America*
[g] *The Fleischer Institute for Diabetes and Metabolism, Albert Einstein College of Medicine, United States of America*
[h] *Department of Pathology, Albert Einstein College of Medicine, 1300 Morris Park Ave., Forchheimer Building, Rm 520, Bronx, NY 10461, United States of America*
[i] *Department of Biochemistry, Albert Einstein, United States of America*
[j] *Thomas J. Long School of Pharmacy, University of the Pacific, Stockton, CA, United States of America*
[k] *Institute for Animal Studies, Albert Einstein College of Medicine, Van Etten Building, Room 463, Bronx, NY 10461, United States of America*
[l] *Department of Pathology, Albert Einstein College of Medicine, 1300 Morris Park Ave., Forchheimer Building 514, Bronx, NY 10461, United States of America*

ARTICLE INFO

Keywords:
Heterotopia
Abnormal neuronal positioning
Neuronal migration defects
De novo dynein heavy chain mutation
Cortical layer-specific transcription factors
Autism spectrum disorder (ASD)

ABSTRACT

Aims: Cytoplasmic dynein heavy chain (DYNC1H1) is a multi-subunit protein complex that provides motor force for movement of cargo on microtubules and traffics them back to the soma. In humans, mutations along the DYNC1H1 gene result in intellectual disabilities, cognitive delays, and neurologic and motor deficits. The aim of the study was to generate a mouse model to a newly identified *de novo* heterozygous DYNC1H1 mutation, within a functional ATPase domain (c9052C > T(P3018S)), identified in a child with motor deficits, and intellectual disabilities.

Results: P3018S heterozygous (HET) knockin mice are viable; homozygotes are lethal. Metabolic and EchoMRI™ testing show that HET mice have a higher metabolic rate, are more active, and have less body fat compared to wildtype mice. Neurobehavioral studies show that HET mice perform worse when traversing elevated balance beams, and on the negative geotaxis test. Immunofluorescent staining shows neuronal migration abnormalities in

Abbreviations: AAA, ATPase domains associated with cellular activities; AMB, Ambulation+ Z Total: Ambulation and Rearing; APC, Adenomatous Polyposis Coli, marker for mature oligodendrocytes; ASD, autism spectrum disorder; Cbl, cerebellum; CNS, central nervous system; CPN, Cortical projection neurons; CTGF, Connective tisue growth factor (CTGF)/cellular communication network factor 2 (CCN2); CUX1, Cut-Like 1, CCAAT Displacement Protein (Drosophila), transcription factor; DAPI, (4′,6-diamidino-2-phenylindole); DYNC1H1, Cytoplasmic dynein heavy chain; GFAP, glial fibrillary acidic protein; HET, heterozygous mice for the mutation proline to serine mutation at amino acid 3018 (P3018S); H&E, hematoxylin and eosin; Iba1, Ionized calcium-binding adaptor molecule 1; MAP2, microtubule-associated protein 2; MBP, myelin basic protein; MFI, mean fluorescent intensity; NeuN/Fox3, Neuronal Nuclear Antigen; P, postnatal day; PAGE-SDS, polyacrylamide sodium dodecyl sulfate gel electrophoresis; P3018S mutation, proline to serine mutation at amino acid 3018; PI, propidium iodide; RER, respiratory Exchange Ratio (O_2 and CO_2 volume); WT, wildtype; *Z*-total, Number of rears.

* Corresponding authors.
E-mail addresses: yongwei.zhang@einsteinmed.edu (Y. Zhang), rstout@nyit.edu (R.F. Stout), jaafar.tindi@einsteinmed.edu (J.O. Tindi), licheng.Wu@einsteinmed.edu (L. Wu), gary.schwartz@einsteinmed.edu (G.J. Schwartz), yair.botbol@einsteinmed.edu (Y.M. Botbol), simone.sidoli@einsteinmed.edu (S. Sidoli), apoojari@PACIFIC.EDU (A. Poojari), tammy.rakowski-anderson@einsteinmed.edu (T. Rakowski-Anderson), bridget.shafit-zagardo@einsteinmed.edu (B. Shafit-Zagardo).

[1] In Memorium. The authors sadly acknowledge the tragic passing of Maider Michelena Beltran De Heredia, September 2023. This publication serves as a reminder of her immense passion for science and life.

https://doi.org/10.1016/j.nbd.2024.106594
Received 29 February 2024; Received in revised form 1 July 2024; Accepted 3 July 2024
Available online 16 July 2024

the dorsal and lateral neocortex with heterotopia in layer I. Neuron-subtype specific transcription factors CUX1 and CTGF identified neurons from layers II/III and VI respectively in cortical layer I, and abnormal pyramidal neurons with MAP2+ dendrites projecting downward from the pial surface.
Conclusion: The HET mice are a good model for the motor deficits seen in the child, and highlights the importance of cytoplasmic dynein in the maintenance of cortical function and dendritic orientation relative to the pial surface. Our results are discussed in the context of other dynein mutant mice and in relation to clinical presentation in humans with *DYNC1H1* mutations.

1. Introduction

Dyneins belong to the family of cytoskeletal motor proteins that convert ATP to mechanical energy to move along microtubules within cells. Dynein functions include spindle-pole organization and nuclear migration during mitosis, positioning and functioning of the endoplasmic reticulum, Golgi apparatus, and nucleus, transport of an array of cargos including proteins, mRNA, endosomes, mitochondria, lysosomes, lipid droplets, perixosomes, autophagosomes, the retrograde transport of vesicles along microtubules, and transport in dendrites and axons in neurons (Kural et al., 2005; Hoang et al., 2017; Hafezparast et al., 2003; Schiavo et al., 2013; Yang et al., 2015; Reck-Peterson et al., 2018; Roberts et al., 2013; Pfister et al., 2006; Driskell et al., 2007; Pilling et al., 2006; Gross et al., 2000; Jordens et al., 2001). Schwann cells and oligodendrocytes require cytoplasmic dynein for proper myelination (Yang et al., 2015; Langworthy and Appel, 2012).

Dynein functions in all cell types, and is composed of multiple subunits which assemble with cytoplasmic dynein heavy chain 1 (DYNC1H1) dimer to form the core of the complex. DYNC1H1 cargo binding requires the dynactin complex (Asante et al., 2014; Schroer, 2004) to enhance processivity and motility along microtubules. The N terminus of the DYNC1H1 is an assembly scaffold for accessory proteins, both structural and regulatory. Roles for DYNC1H1 in mitotic and post-mitotic motility and the regulation of neuronal homeostasis highlights the reported neuropathies and CNS malformations observed in patients with *DYNC1H1* mutations (Hoang et al., 2017; Schiavo et al., 2013; Lipka et al., 2013; Moller et al., 1993; Romero et al., 2023). The *Dyc1h1* gene contains 78 exons and has been mapped to human chromosome 14q32.31, and mouse chromosome 12.

DYNC1H1 is ~532 kilodaltons. While pairs of dynein heavy chain homodimerize *via* its N-terminal tail domains to form the core of the dynein complex, the C-terminal motor domain spans amino acids 1846–4646 (Poirier et al., 2013), containing six ATPases domains associated with cellular activity domains (AAA domains). Of the six AAA+ domains only AAA1, AAA3, AAA4, can hydrolyze ATP. The AAA4 domain controls the priming stroke of the motion-generating linker, which connects the dimerizing tail of the motor to the AAA+ ring. Before ATP binds to AAA4, dynein remains incapable of generating motion. When AAA4 is bound to ATP, the gating of AAA1 by AAA3 prevails and dynein motion occurs (Liu et al., 2020).

Missense mutations in the cytoplasmic dynein stem domain cause the mouse phenotypes *LOA*, *Cra*, and *Swl*, which display defective retrograde transport leading to neurodegeneration and errors in neuronal migration, and in axon growth (Hafezparast et al., 2003; Schiavo et al., 2013). Dync1h1 HET mutations in mice Loa (F580Y) and Cra (Y1055C) were generated during chemical mutagenesis (Hafezparast et al., 2003; Chen et al., 2007; Tynan et al., 2000; Habura et al., 1999). The mutant Swl (G1040–T1043delinsA) was induced by radiation (Chen et al., 2007; Duchen, 1974). Mutations in *DYNC1H1* occur in several nervous system disorders including CNS defects in neuronal migration and axonal growth (Hafezparast et al., 2003; Poirier et al., 2013; Vissers et al., 2010; Willemsen et al., 2012; de Ligt et al., 2012; Harms et al., 2012; Ori-McKenney and Vallee, 2011), a combined involvement of motor and sensory motor deficits in Charcot-Marie-Tooth disease and Spinal muscular atrophy with lower extremity predominance (Weedon et al., 2011; Li et al., 2022). A zebrafish *DYNC1H1* mutation resulting in a truncated protein has trafficking defects (Insinna et al., 2010).

In the central nervous system (CNS), newly born neurons extend a process from the soma toward the cortical plate, and the cell body moves following the direction of this process in a saltatory way. Purkinje cell migration follows a similar pattern during cerebellar development. Dynein, together with its other components in the complex, is responsible for coupling movement of the soma to the extension of the process (Tsai et al., 2007).

We have generated a new Dync1h1 mouse model with a patient-specific point mutation within the third functional ATPase domain AAA4 (c9052C > T (exon 46; P3018S) located adjacent to the stalk within the motor domain. The mutation was modeled after a *de novo* autosomal dominant missense mutation identified in a child following whole exome sequencing. The mutation is not found in his healthy parents or siblings, and is considered an autosomal dominant since he has one normal copy of the gene. The child was seen at The Rose F. Kennedy Intellectual Developmental Disabilities Research Center, at Albert Einstein College of Medicine. He presented with deficits in motor coordination, and cognitive problems that include deficits in planning and learning, and is on the autism spectrum. We have determined that in mice this heterozygous (HET) point mutation DYNC1H1 c9052C > T (P3018S) results in neural deficits through defects in neuronal orientation and migration that account for motor and learning deficits.

2. Materials and methods

2.1. Mice

The knockin heterozygous (HET) mice with a point mutation c9052C > T in the Dync1h1 gene were generated on a C57BL/6 J background (The Jackson Laboratory; Bar Harbor, ME) in The Gene Modification Facility within the Cancer Center at Albert Einstein College of Medicine. The DYNC1H1 mouse model was constructed using CRIPSR/Cas9 mediated genome editing (Yang et al., 2013). In brief, two guide RNAs (gRNAs) targeting intron 46 (targeting sequence: TGCCTCCTCACCTCTCGATG AGG) and intron 47 (targeting sequence: AGTGACCCTCGATGGAGTCC AGG) of the mouse *DYNC1H1* gene respectively, a single stranded homology directed repair donor DNA carrying the desired *DYNC1H1* mutation and Cas9 protein was injected into the fertilized eggs of C57BL/6 J mice, and then the injected fertilized eggs were transferred to the pseudopregnant CD1 female mice for producing pups. The resulting progeny were screened by DNA sequencing to identify correctly targeted founder (F0), F1 and F2 mice. DNA sequencing confirmed that the mice are heterozygous for the point mutation. All proposed studies were performed in accordance with the recommendations in the Guide for the Care and Use of Laboratory Animals of the National Institutes of Health and the Albert Einstein College of Medicine IACUC guidelines. The mutation was confirmed by DNA sequencing (Fig. 1). DYNC1H1 heterozygous mice are viable and were crossed with both male or female heterozygous and WT mice (C57BL/6-J) to obtain HET and WT littermates. No homozygous pups have been born during the over 2 years of HET x HET matings. A chi-square test were performed to examine differences between observed and expected offspring genotype frequencies in HET X HET or WT X HET matings, and the associations of HET X HET or WT X HET matings with offspring genotypes. Of 34 pups born from HET X WT matings, 18 (52.9%) were

heterozygous and 16 (47.1%) were WT. There was no difference in observed and expected offspring genotype frequencies in HET x WT matings ($p = 0.732$). Of 124 pups born from HET X HET matings, 68 (54.8%) were heterozygous and 56 (45.2%) were WT. No homozygous pups were obtained from any matings. The observed WT, heterozygote and homozygote frequencies were significantly different from the expected wild-type, heterozygote and homozygote ratio of 31:62:31 ($p < 0.001$) or the expected wild-type and heterozygote ratio of 41:82 assuming the homozygotes are missing ($p = 0.005$). A chi-square test with p value =0.844 indicates that the genotype of the offspring is not affected by the mating pairs.

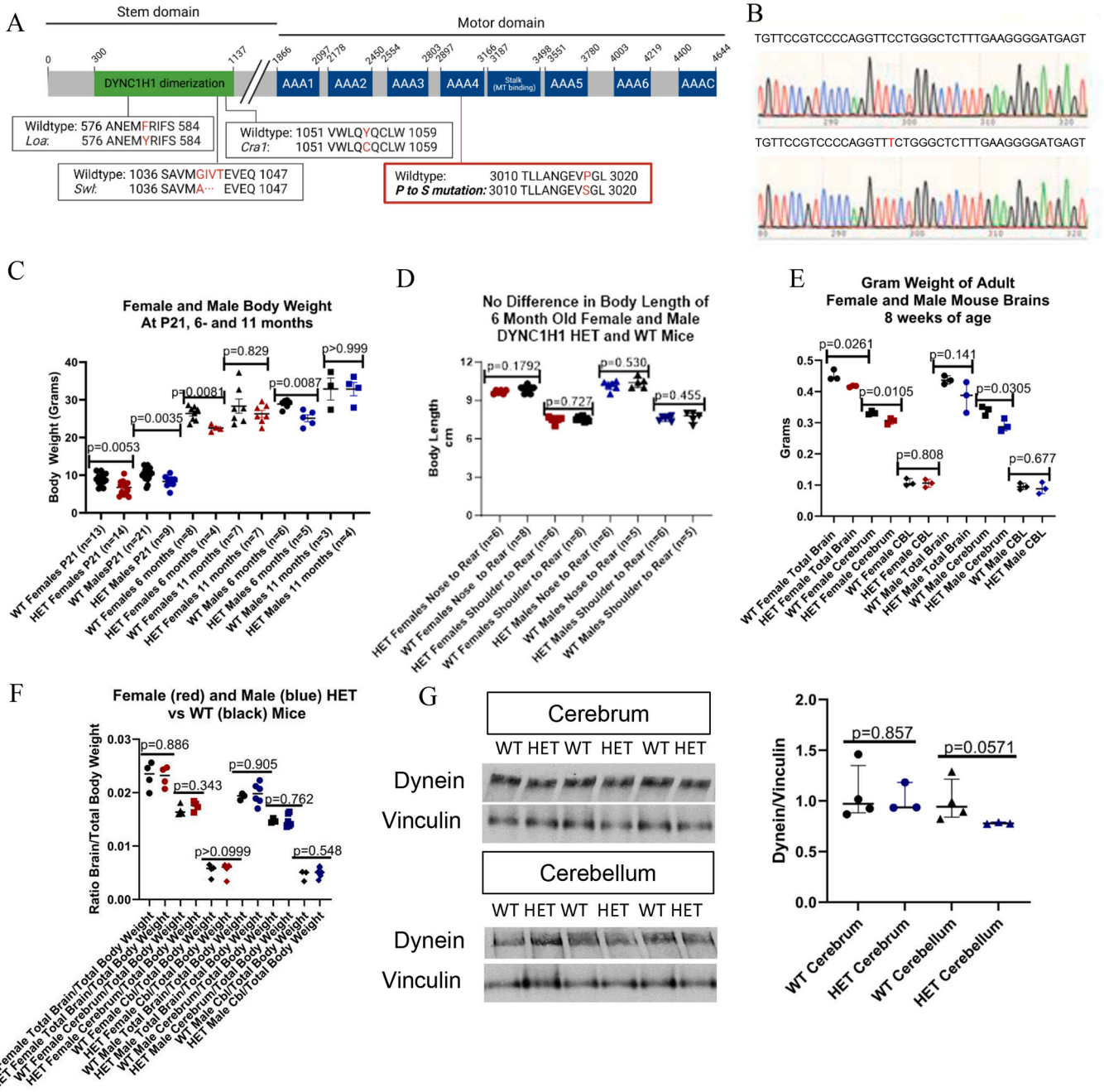

Fig. 1. Mice with a heterozygous (HET) DYNC1H1 mutation at P3018S weigh less and have smaller brain weight during early postnatal development.
A. Schematic representation of DYNC1H1 and its domains, with the reported mouse and human mutations (Banks and Fisher, 2008). Shown in blue rectangles are the single letter amino acids for the mouse and human mutations (uniport.org; Q9JHU4 mouse; Q14204 human). The red rectangle shows the human proline to serine mutation at 3018 within the AAA4 ATPase domain. B. Sequence analysis demonstrating the HET Dync1h1 mutation resulting in the P/S amino acid substitution. C. Reduced body weight in HET mice at postnatal day 21 (P21). Female WT ($n = 13$; black) and HET ($n = 14$; red) and male WT ($n = 21$; black) and HET ($n = 9$; blue) pups were weighted upon weaning at P21. At 6 months of age HET female and male pups weigh less than WT, but not at 11 months of age. Median ± interquartile range, Mann Whitney U test. D. No difference in body length of adult HET and WT mice. Mann Whitney U test. E. Brain weight is reduced in HET mice relative to WT young adult mice ($n = 3$/group). F. No differences in the ratio of brain/body weight of adult HET and WT mice. Mann Whitney U test. G. Western blot analysis shows that when normalized to vinculin, DYNC1H1 is unchanged in the cerebrum and cerebellum of adult HET and WT males. Quantification shows WT (n = 3) and HET ($n = 4$) males $p > 0.05$, Mann Whitney U test. (For interpretation of the references to colour in this figure legend, the reader is referred to the web version of this article.)

2.1.1. Thy1YFP+(layer 2–6) WT and DYNC1H1 c9052C ≥ T (P3018S) heterozygous mice

Thy1YFP+(layer 2–6) mice (003709; The Jackson Laboratory; Bar Harbor, ME) were crossed with DYNC1H1 heterozygous mice and WT and HET pups were confirmed by the genotyping service Transnetyx (Cordova, TN) using duplexed PCR Thy1YFP primers established at The Jackson Laboratory, and Dync1h1 HET primers.

2.2. Brain analysis

For analysis of WT and HET brains, 50 μm sections of entire brains were cryostat-sectioned and microscopically examined ($n \geq 20$ animals/group). The cerebrum was sectioned coronally, and the cerebellum was sectioned in coronal or sagittal planes. Examination of lumbar spinal cords was performed on 10 μm paraffin-embedded sections. For lamination defects, multiple brain regions of male and female mice were examined at P14, P21, and 7–12 weeks of age. For all brains, a propidium iodide or Nissl stain was performed at least every 10 serial sections. For examination of inverted neurons, MAP2 and NeuN staining were performed, and the number of inverted neurons was examined per 20× field centered on layers I-II. While no inverted neurons were observed in the WT mice, examination of HET mice found 1–2 inverted neurons/x20 field. A minimum of three mice/group were examined for all performed studies.

2.3. MicroCT to analyze the brain and ventricles in WT and HET mice

High resolution MicroCT (Bruker SkyScan1173) was performed to image adult mouse brains and the ventricles using iodine-based contrast (Kastner et al., 2020). Briefly, after fixation in 4% paraformaldehyde for 3–5 days, brains were submerged in 1% iodine solution for at least 1 week to allow for full penetration into brain. Brains were secured in 4%

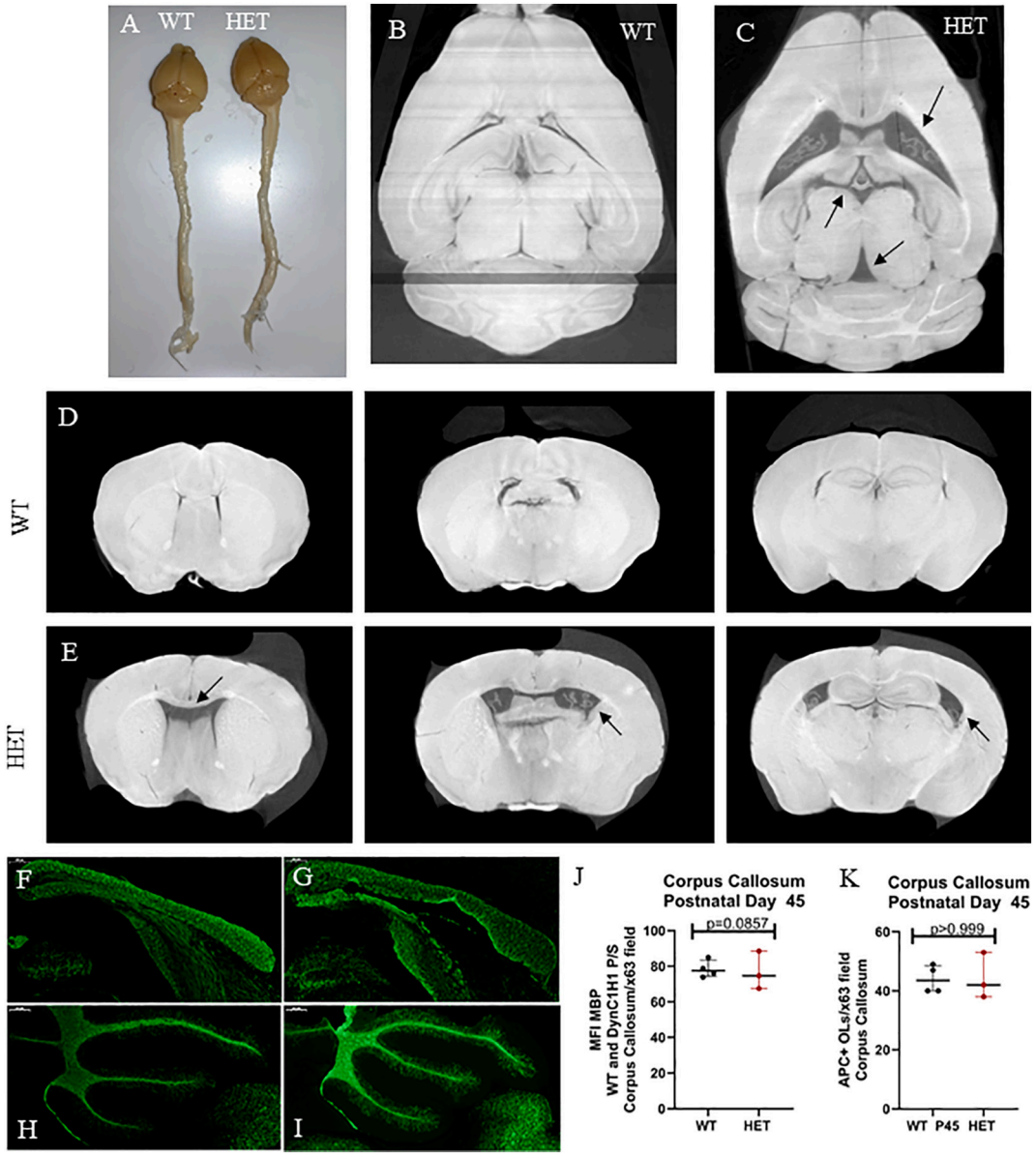

Fig. 2. HET mice have enlarged ventricles.
A. Gross anatomy of WT and HET brains and spinal cords do not appear different. B,C. MicroCT imaging of WT and HET male brains in the horizontal plane. D,E. MicroCT shows coronal images of representative WT and HET cortices visualized from anterior to posterior. MBP immunofluorescent staining of cortex at the corpus callosum and cerebellum of WT (F,H) and HET (G,I) mice at P21 (SMI99, 1:1000, Millipore, NE1019). There were no differences in MBP MFI (J) and the number of mature oligodendrocytes (K) within the corpus callosum.

agarose in plastic tubes and scanner set to 80 kV and 100 μA and at 12.18 μm pixel size. Image stacks were visualized in ImageJ. Based on microCT analyses, and light microscopy of multiple 50 μm coronal brain sections through the cerebrum, we determined that 14/21 (67%) of mice had enlarged ventricles (Fig. 2).

2.4. Metabolic testing

Metabolic testing was performed continuously over a 5-day period using metabolic chambers (Columbus Instruments, Columbus OH). Adult female and male mice were tested. The method scores counts as ambulation (AMB) when the animal traverses the cage, breaking a series of IR beams in sequence. Repeated interruptions of the same IR beam do not incur ambulatory counts. All beam interruptions are scored as Total Activity. Statistical analyses were done on days 3–5. The first two days are habituation and are not included in the analysis.

2.5. EchoMRI™ analysis

EchoMRI™ (EchoMRI™; Houston, TX) analyzes body composition measuring lean/muscle, fat, and water masses on live mice. Lean and fat are added to get total body weight. The data is presented as % Fat/Total Body Weight.

2.6. Neurobehavioral testing

Behavioral testing of WT and HET DYNC1H1 male and female mice was conducted during the light phase except for the parallel floor plate assay. Researchers conducted tests blinded to the genotypes. The specific statistical test is indicated in the figure legends. Mice were subjected to the following behavioral tests.

2.6.1. Negative geotaxis

Mice were placed on a metal rack and turned 90^{o} downward so the brain is toward the floor. The time (seconds) it takes for the mice to rotate head up is recorded (Ray et al., 2017).

2.6.2. Hindlimb clasping assay (Guyenet et al., 2010; Zhu et al., 2016)

Mice were suspended by the tail and the extent of hindlimb clasping was observed for 10 s. If both hindlimbs were splayed outward away from the abdomen with splayed toes, a score of 0 was given. If one hindlimb was retracted or both hindlimbs were partially retracted toward the abdomen without touching it and the toes were splayed, a score of 1 was assigned. A score of 2 was assigned if both hindlimbs were partially retracted toward the abdomen, without touching each other. A score of 3 was assigned when the mice fully clasped both hindlimbs and they touched the abdomen. This test was repeated on the same mice on different days and at different times to check for consistency. It was performed in mice 3–7 weeks of age, 3–4-month-old mice, and 6 month and 1-year old mice.

2.6.3. Elevated balance beams test

14 HET mice and 25 WT mice were evaluated on three different diameter balance beams: 1, 0.75 and 0.5 in. The number of slips was measured as the mice traversed the beams. Time was not considered (Ray et al., 2017).

2.6.4. Parallel floor test

WT and HET mice were assessed on the parallel rod floor test during the dark cycle, as previously described (Mayoral-Palarz et al., 2022; Kamens and Crabbe, 2007) using a four-enclosure apparatus (Stoelting, Wood Dale, IL). Briefly, the assay was performed for 10 min during which the number of errors and the total distance traveled was automatically recorded for each mouse. Each mouse completed a single 10 min session per day over 3 consecutive days. The number of foot slips (#) was calculated for each mouse for each session by dividing the total of number of errors by the total distance traveled (cm). The data is presented as the # of foot slips/cm. Mice were acclimated to the assay on day 1 and tested on days 2 and 3. Motor performance was assessed by averaging the # of foot slips/cm for days 2 and 3 for each mouse.

2.6.5. Open arm y maze

WT and HET mice were placed in the center of the maze box and allowed to freely explore the 3 open arms each at a 120-degree angle to each other. The number of times the mouse explored each of the three arms, and the total times all four paws were within an arm was recorded at 2- and 5-min. The number of explorations of all arms was compared for male and female mice.

2.7. Western blot analysis

Total brains were weighed, and the cerebrum and cerebellum were dissected and weighed. Brain tissues were disrupted and lysed in Urea 8 M. Total protein was quantified by Bradford and loaded onto 7% or 12% PAGE-SDS gels. For analysis of dynein, proteins were separated on a 7% SDS polyacrylamide gel and transferred to nitrocellulose membrane. Nitrocellulose blots were incubated with primary antibodies specific for dynein heavy chain 1 (α-DYNC1H1; 1:1750; rabbit polyclonal; Proteintech cat# 12345–1-AP; Rosemont, IL), and vinculin, routinely used as a housekeeping protein (vinculin (7F9); dilution 1:10,000: mouse monoclonal IgG1; Santa Cruz Biotechnology cat# sc-73,614; 1:1000; 117 kDa, Paso Robles, CA); or MBP (SMI99; 1:1000, Millipore) and β-actin (Sigma, AB6276; 1:15,000). Bands were quantified using ImageJ from at least 2 different exposures for each blot.

2.8. Antibodies for immunofluorescence staining

NeuN is predominantly nuclear with some perinuclear staining of neurons (NeuN; Millipore ABN78, MAB377; 1:1000). Calbindin stains Purkinje cells (anti-calbindin; dilution 1:500; mouse monoclonal IgG1. EnCorBio, MCA-5A9); Cut-Like 1, CCAAT Displacement Protein (Drosophila) transcription factor (CUX1; 1:500, Santa Cruz Biotechnology, B10, sc-514,008) and Connective tisue growth factor (CTGF)/cellular communication network factor 2 (CCN2) (Santa Cruz Biotechnology, E-5, sc-365,970) are nuclear transcription factors. Microtubule-associated protein 2 (MAP2; Biosensis, chicken polyclonal antibody, C-1382-50, and 1:500; chicken polyclonal; Abcam cat#ab92434) is predominantly expressed in the neuronal cell body and dendrites. Neurofilament protein SMI32 identifies neurons and dendrites in spinal cord (1:1000; mouse monoclonal IgG1, Millipore cat#NE1023); Neurofilament protein SMI3I identifies healthy axons (1:1000; mouse monoclonal IgG1, Millipore cat#NE1022); Myelin basic protein (MBP; SMI99,1:1000, Millipore cat #NE1019) was used to stain myelin. Glial fibrillary acidic protein (anti-GFAP dilutions 1:200–1:500; mouse monoclonal IgG1, Milllipore; astrocytic marker). Iba1 rabbit polyclonal antibody (1:500 dilution; WAKO Chemicals USA, cat #019–19,741). **Secondary antibodies** were goat-anti-Rabbit Alexa Fluor™ 488 (dilution 1:1000, Thermo Fisher Scientific cat#A-11008), goat-anti-Mouse IgG2b Alexa Fluor™ 568 (dilution 1:1000, Thermo Fisher Scientific cat#A-21144) and goat-anti-Mouse IgG1 Alexa Fluor™ 568 (dilution 1:1000, Thermo Fisher Scientific cat#A-21124).

2.9. Immunofluorescence staining

Brain and spinal cords were dissected from mice following transcardial perfusion with 4% paraformaldehyde, placed in paraformaldehyde for 48 h, and then transferred to 30% sucrose.

2.9.1. Spinal cords

For sectioning, lumbar portions of spinal cords were embedded in paraffin and serial cross- sections (10 μm thick) were cut in a microtome. Sections were deparaffinized, serially hydrated (xylene, 100% ethanol,

95% ethanol, 80% ethanol, and 1× TBS) and boiled for 7 min on high, followed by power 7 for an additional 7 min in a microwave.

2.9.2. Brains

Brains were embedded in OCT (Sakura Tissue-Tek; Torrance, CA) and serial 50 μm cross sections were cut on a cryostat. Free- floating sections were permeabilized for 30 min in 3% H_2O_2, 0.25% Triton X100 in 1× TBS. Sections were blocked in 5% non-fat milk plus 5% goat serum for 1 h at room temperature. Primary antibodies were diluted in 5% non-fat milk 1× TBS and incubated overnight at 4 °C. Sections were incubated with secondary antibody diluted in non-fat milk for 1 h at room temperature. Mounted sections were air dried and covered with 1.5 mm coverslips. Mounting medium ProLong™ Gold antifade reagent with DAPI (Invitrogen by Thermo Fisher Scientific cat#P36935, OR, USA).

2.10. Histologic grading of spinal cords

Slides were blinded and at least three sections of the lumbar spinal cord for each animal were assessed by two individuals; the number of animals used for each experiment is indicated in the figure legends. The Mann–Whitney *U* test was used to evaluate statistical significance.

Histological sections were graded on a scale of 0–3 as previously described (Ray et al., 2017). For GFAP+ and Iba1+ staining, cross-sectional spinal cords were scored on a 0–3 inflammatory scale where a score of 0 is the equivalent staining observed in the naïve WT mice. A score of 1 = indicative of mild inflammation, 2 = moderate inflammation, 3 = severe inflammation throughout the cord. All WT and HET spinal cords examined scored 0 with no differences between WT and HET spinal cord for GFAP and Iba1. We did not observe changes in the shape of the astrocytes or microglia indicative of activation and inflammation, and there was no increase in their proliferation. Further assessment (Harrison et al., 2019; Gibson-Corley et al., 2013) of the glial activation state, shape, and GFAP+ or Iba1+ glia in ventral spinal cord was examined (150× field, 3DHistec Panoramic 250 Flash III P250 slide scanner) evaluating glia as a 1 for a resting state, to 5 to a fully activated state. Changes in glial morphology were considered, as well as the intensity of the Iba1 and GFAP protein. Several sections from 3 WT and 3 HET male and female mice were examined.

For relative changes in myelination and to assess decreased MBP staining in spinal cords, scores were assigned as follows: 0 = MBP immunoreactivity observed in multiple naïve WT lumbar spinal cord sections. A score of 1 = mild demyelination consisting of a few small white matter areas within the cord parenchyma, 2 = moderate demyelination consisting of at least two demyelinated regions of the cord. Examination of 3 WT and 3 HET male and female mice did not show any regions with loss of MBP within the cord parenchyma.

2.11. Examination of neurons in coronal sections of lumbar spinal cord

H&E, SMI32 and NeuN were used to determine whether there was neuronal loss in the ventral spinal cord. At least three coronal lumbar spinal cords from WT and HET mice were examined and a minimum of three sections/mouse were evaluated. There was no significant difference in the observed number of motor neurons in total ventral lumbar spinal cord in mice at 9 weeks of age.

To determine whether there was axonal damage in the ventral lumbar spinal cord, coronal sections ($n = 3$) were evaluated for SMI32+ axonal swellings (>3 μm) in the white matter at multiple X20 fields. Scores were assigned as follows: 0 = no SMI32+ axonal swellings in ventral white matter, in the WT and HET mice. A score of 1 = ≤10 SMI32+ swellings in white matter, 2 = 10–20 SMI32+ swellings. All WT and HET spinal cords axons scored 0 with no differences between WT and HET mice. Further, staining of healthy axons were examined in the lumbar spinal cord using the phosphoneurofilament protein antibody SMI31, specific for axon. Following examination of multiple sections with both SMI31 and SMI32, we were able to confirm that there was no axonal loss or axonal swelling in the HET lumbar spinal cord relative to the WT mice.

2.12. NanoLC-MS/MS

Method for liquid chromatography coupled online with tandem mass spectrometry (nanoLC-MS/MS) to determine how the mutation alters the abundance of specific neuronal proteins. Total protein from the dissected cerebrum and cerebellum was homogenized from 9-week old male and females ($n \geq 5$/group) using a buffer containing 5% SDS, 5 mM DTT and 50 mM ammonium bicarbonate (pH = 8.0), and left on the bench for about 1 h for disulfide bond reduction. Samples were then alkylated with 20 mM iodoacetamide in the dark for 30 min. Afterward, phosphoric acid was added to the sample at a final concentration of 1.2%. Samples were diluted in six volumes of binding buffer (90% methanol and 10 mM ammonium bicarbonate, pH 8.0). After gentle mixing, the protein solution was loaded to an S-trap filter (Protifi) and spun at 500 *g* for 30 s. The sample was washed twice with binding buffer. Finally, 1 μg of sequencing grade trypsin (Promega), diluted in 50 mM ammonium bicarbonate, was added into the S-trap filter and samples were digested at 37 °C for 18 h. Peptides were eluted in three steps: (i) 40 μl of 50 mM ammonium bicarbonate, (ii) 40 μl of 0.1% TFA and (iii) 40 μl of 60% acetonitrile and 0.1% TFA. The peptide solution was pooled, spun at 1000 *g* for 30 s and dried in a vacuum centrifuge.

Prior to mass spectrometry analysis, samples were desalted using a 96-well plate filter (Orochem) packed with 1 mg of Oasis HLB C-18 resin (Waters). Briefly, the samples were resuspended in 100 μl of 0.1% TFA and loaded onto the HLB resin, which was previously equilibrated using 100 μl of the same buffer. After washing with 100 μl of 0.1% TFA, the samples were eluted with a buffer containing 70 μl of 60% acetonitrile and 0.1% TFA and then dried in a vacuum centrifuge.

Samples were resuspended in 10 μl of 0.1% TFA and loaded onto a Dionex RSLC Ultimate 300 (Thermo Scientific), coupled online with an Orbitrap Fusion Lumos (Thermo Scientific). Chromatographic separation was performed with a two-column system, consisting of a C-18 trap cartridge (300 μm ID, 5 mm length) and a picofrit analytical column (75 μm ID, 25 cm length) packed in-house with reversed-phase Repro-Sil Pur C18-AQ 3 μm resin. Peptides were separated using a 60 min gradient from 4 to 30% buffer B (buffer A: 0.1% formic acid, buffer B: 80% acetonitrile +0.1% formic acid) at a flow rate of 300 nl/min. The mass spectrometer was set to acquire spectra in a data-dependent acquisition (DDA) mode. Briefly, the full MS scan was set to 300–1200 m/z in the orbitrap with a resolution of 120,000 (at 200 m/z) and an AGC target of 5x10e5. MS/MS was performed in the ion trap using the top speed mode (2 s), an AGC target of 1x10e4 and an HCD collision energy of 35.

Proteome raw files were searched using Proteome Discoverer software (v2.4, Thermo Scientific) using SEQUEST search engine and the SwissProt mouse database (updated March 2024). The search for total proteome included variable modification of N-terminal acetylation, and fixed modification of carbamidomethyl cysteine. Trypsin was specified as the digestive enzyme with up to 2 missed cleavages allowed. Mass tolerance was set to 10 pm for precursor ions and 0.2 Da for product ions. Peptide and protein false discovery rate was set to 1%. Proteins were log2 transformed, normalized by the average value of each sample and missing values were imputed using a normal distribution 2 standard deviations lower than the mean. After that, protein abundances were reverted from log2 to simplify representation. Statistical regulation was assessed using heteroscedastic *t*-test (if p-value <0.05). Data distribution was assumed to be normal but this was not formally tested. p-values in Supplementary Fig. 1 are represented as regular p-values (not log transformed).

2.13. Statistical analysis

Statistical analysis was performed with GraphPad Prism version 10.1.2 software. To analyze significance, a Mann–Whitney *U* test was

performed, and data is shown as median plus interquartile range. Significance for relative scales, such as GFAP, Iba1 and MBP in Fig. 3 were assessed for significance by the Mann–Whitney *U* test; results of these tests were all non-significant and all histological scaling scores were 0 for GFAP, Iba1 and MBP for WT and HET mice (see above for scores). Student's *t*-test was performed for parametric two-group comparisons. Error is represented as SD. Significant following nanoLC-MS/MS is indicated above.

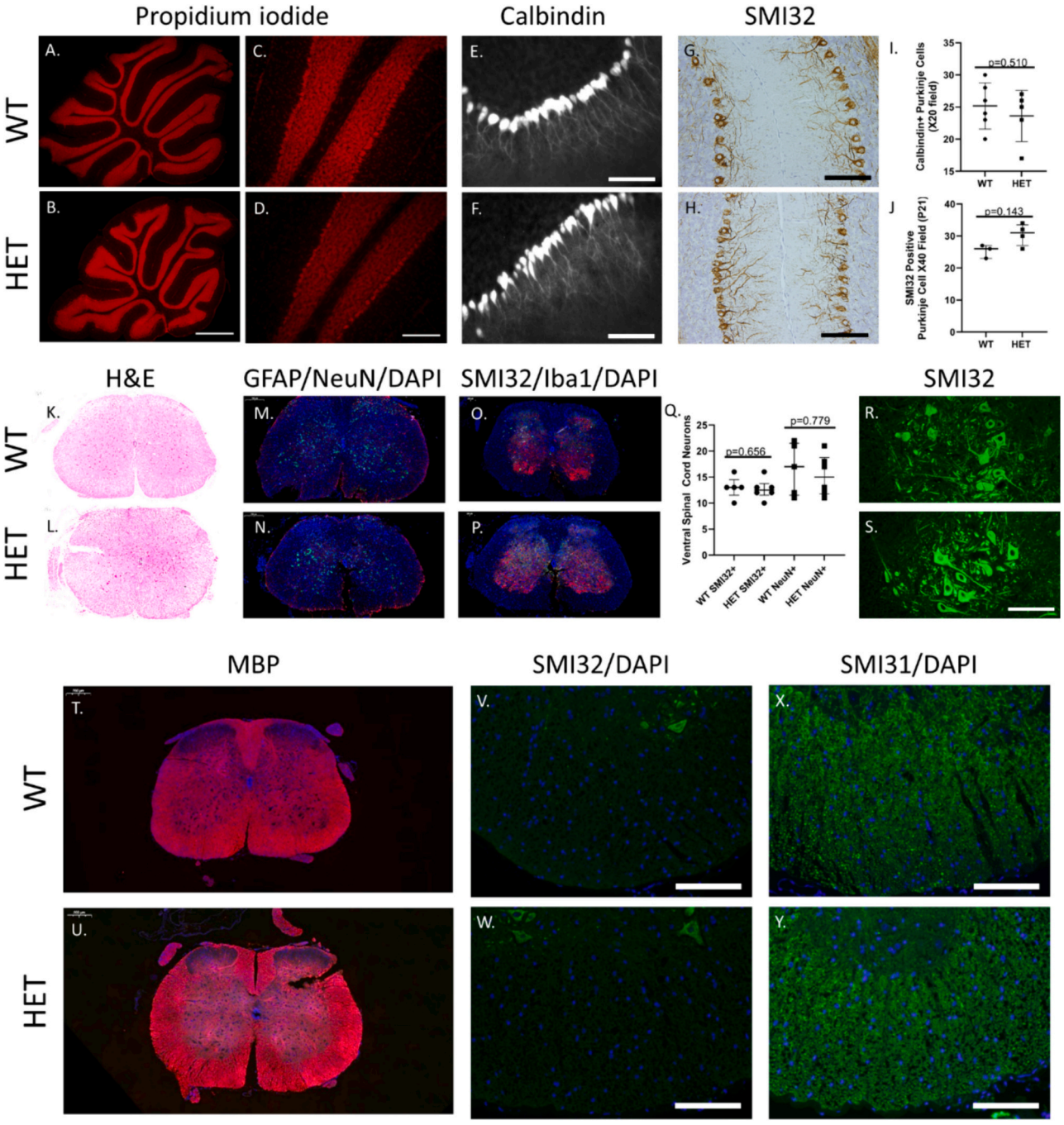

Fig. 3. No differences in cerebellum or spinal cord in WT and HET mice.
A-D. Propidium iodide staining of WT (A,C) and HET (B, D) cerebella. Staining of free-floating sections of cerebellum with antibodies to calbindin and neurofilament protein SMI32 showed no differences in the number of calbindin+ purkinje cells/field (E,F,I) and SMI32+ purkinje cells/field (G,H,J). Median with interquartile range, Mann Whitney *U* test. Representative 10 μm coronal sections of lumbar spinal cord stained with H&E (*K,L*). Spinal cord immunofluorescent staining with neuronal markers NeuN+ neurons (M,N; green), SMI32+ neurons (O,P; red) and DAPI (M-P; blue). M,N. GFAP staining (red). O,P. Iba1 staining (green). Q. No difference in the number of SMI32+ or NeuN+ neurons in ventral lumbar spinal cord. Median with interquartile range, Mann Whitney *U* test. R,S. SMI32+ WT (R) and HET (S) ventral spinal cord neurons at higher magnification. T,U. MBP immunofluorescent staining in WT (T) and HET (U) ventral spinal cord. V,W. SMI32+ (green) and DAPI+ (blue) staining of WT (V) and HET (W) ventral lumbar spinal cord white matter shows no SMI32+ swollen axons or spheroids. X,Y. Phosphoneurofilament antibody SMI31 (green) and DAPI (blue) staining of healthy axons in ventral lumbar spinal cord white matter of WT (X) and HET (Y) mice. Scalebars (in microns): A-B = 800; C-D = 160; *E*-H, K—P, T-U = 200; R-S, V-Y = 100. (For interpretation of the references to colour in this figure legend, the reader is referred to the web version of this article.)

3. Results

3.1. Characterization of heterozygous (HET) knockin cytoplasmic dynein heavy chain, DYNC1H1, mice with a P3018S point mutation

Knockin mice containing the DYNC1H1 c9052C > T (P3018S) mutation were generated on a C57BL/6 J background (Fig. 1A, B). HET mice with the P/S mutation breed well and over 75 HET pups have been born. In over 15 independent mating cages no homozygous pups were obtained, suggesting that homozygosity is lethal. HET X HET litter sizes are normal for the first few litters, but the number of pups per litter decreases to 2–3 pups as the mom nears 8 months of age.

Perinatal examination of the fur, righting, eye opening, teeth eruption, and ears separating from the head of HET and WT pups are all normal and consistent with the perinatal developmental period (Hill et al., 2008). Age- and sex-matched littermates weighed upon weaning, at postnatal day 21 (P21), show a reduction in the body weight of HET pups in both sexes relative to WT littermates (Fig. 1C). The difference in body weight is apparent at earlier and later time points, and is independent of litter size. While still apparent at 6 months of age, the difference in body weight is not significantly different by 11 months of age.

Necropsy of pups at P21 and young adult mice (4–5 months of age) did not detect overt differences in the appearance of the heart, lungs, liver, kidneys, intestines, and spleen. At 6 months of age, we measured the body length of male and female WT and HET mice to determine whether the difference in body weight affected maturation to adulthood length. Mice were measured from nose to rear, and shoulder to rear. There was no difference in the body length of WT and HET male and female mice (Fig. 1D). When the brains of WT and HET mice were weighed and examined at 8 weeks of age, we determined that the cerebrum of HET male and female mice weighed significantly less than WT littermates; whereas the cerebellum weighed the same (Fig. 1E). When brain weight was normalized to the total body weight significance was not observed (Fig. 1F). Protein homogenates prepared from adult mice determined that the amount of dynein normalized to vinculin or normalized to total protein was the same in both the cerebrum and the cerebellum (Fig. 1G, Supplemental Fig. 1A).

Macroscopic examination of brain and spinal cord of pups at 9 weeks of age appeared grossly normal (Fig. 2A). However, following iodine staining, and upon imaging with MicroCT and sectioning, it was noted that relative to WT littermates (Fig. 2B,D), ~67% of the HET mice had ventriculomegaly (Fig. 2C,E). In particular, we observed obvious enlargement throughout the ventricular system (black arrows in Fig. 2C, E) as well as disruption of the septal nuclei, which normally is present in between the lateral ventricles. As shown in Fig. 2E, the lateral ventricle of each hemisphere were observed connecting and displacing midline tissue.

To determine whether myelination was compromised, nitrocellulose blots containing protein homogenates from WT and HET cerebrum and cerebellum were quantified following incubation with myelin basic protein (MBP). When normalized to total protein, there was no difference in the amount of MBP in WT and HET cerebrum and cerebellum (Supplementary Fig. 1B). Immunofluorescent staining of WT and HET corpus callosum (Fig. 2F,G) and cerebellum (Fig. 2H,I) were consistent with the western blot analysis. Analysis of the corpus callosum showed no significant difference in MBP mean fluorescent intensity (MFI; Fig. 2J), and the number of mature APC+ oligodendrocytes in WT and HET mice (Fig. 2K).

We used mass spectrometry as another approach to quantify protein level changes in DYNC1H1 and MBP normalized to total protein in both male and female mice. NanoLC-MS/MS for both the cerebrum and cerebellum and for both sexes, revealed no significant differences between WT and HET mice similar to our observations using western blot analyses (Supplementary Fig. 1C).

Multiple histological approaches of 50 μm sagittal sections of WT and HET cerebellum did not show differences in lobule formation, lamination, or other major organizational changes. Fig. 3 shows representative propidium iodide stained sections of the cerebellum showing the lobules (Fig. 3A,B), and aligned calbindin+ and SMI32+ labeled Purkinje cells from WT and HET (Fig. 3C-H) mice at higher magnification. Quantification of the number of calbindin+ and SMI32+ Purkinje cells revealed no differences between WT and HET mice (Fig. 3I-J).

3.2. The spinal cords of WT and HET littermates show no significant difference in neurons, astrocytes, microglia, and MBP

Motor neuron degeneration is reported in some DYNC1H1 missense strains of mice (Hafezparast et al., 2003). We examined hematoxylin and eosin (H&E) staining of 10 μm coronal sections of ventral lumbar spinal cords from WT and HET mice (Fig. 3K,L). Immunostaining with the nuclear/perinuclear marker NeuN revealed normal motor neurons in WT and HET mice (Fig. 3M,N green). Staining with the astrocyte marker GFAP (Fig. 3M,N; red) showed no astrogliosis in WT or HET spinal cords. Staining with the microglial marker Iba1 (green) showed no microgliosis in the HET spinal cord (Fig. 3O,P). All WT and HET GFAP+ astrocytes and Iba1+ microglia were considered resting with the staining predominantly within the cell body and 1–2 simple, slender process extensions (Harrison et al., 2019; Gibson-Corley et al., 2013). Intense staining and multiple processes consistent with reactive astrocytes or ameboid activated microglia were not observed.

Neurofilament staining of neurons with antibody SMI32+ (red) did not show a difference in large motor neurons (Fig. 3O,P). Quantification of NeuN+ and SMI32+ neurons in WT and HET ventral lumbar spinal cord did not detect significant difference in the number of neurons (Fig. 3Q, x40 field). SMI32 immunostaining of additional ventral spinal cord sections is shown at higher magnification (Fig. 3R,S; green). MBP immunofluorescent staining was equivalent in WT and HET mice (Fig. 3T,U). Examination of the white matter tracks in the ventral spinal cord did not show SMI32+ axonal swellings or spheroids indicative of axonal damage (Gruber et al., 2014) in WT or HET sections (Fig. 3V,W). Adjacent sections incubated with the phospho-neurofilament antibody SMI31, indicative of healthy axons, showed a similar axonal pattern in WT and HET within ventral white matter spinal cord (Fig. 3X,Y).

3.3. Metabolic and EchoMRI™ analysis show differences in HET metabolism relative to WT littermates

Since HET pups weighed less than WT pups, we measured the daily energy expenditure to assess differences in metabolic states and energetic needs in a Metabolic chamber (Columbus Instruments; Columbus, OH; Fig. 4). Daily energy expenditure includes energy spent on basal metabolism, and on physical activity. Heat is derived by assessment of the oxygen-carbon dioxide exchange that occurs in the metabolic process. The relationship between the volume of gas consumed (oxygen) and the volume produced (carbon dioxide) reveals the energy content of the foodstuff utilized by the subjects. The ratio of O_2 consumption and CO_2 production is the Respiratory Exchange Ratio (RER; Fig. 4B). Ambulation (AMB) shows the movement of the mice within the cage, measured by disruption of the infrared beams and *Z*-total determines the number of rears, together these parameters show the activity of the WT (black bars) and HET (white bars) mice (Fig. 4C). Metabolic testing shows a significant increase in energy expenditure (EE) and RER (O_2 and CO_2 volume) in HET mice relative to WT indicating that HET mice expend more energy over a 5-day period that covers both the light cycles when mice are more inactive, and dark cycles when mice are most active. EchoMRI™ (Houston, TX) show that HET mice have less fat and more lean muscle relative to total body weight when compared to WT littermates (Fig. 4D,E). Female HET mice had significantly less fat, while there was a trend toward less fat in HET males. To determine whether mice at 4–5 months of age have differences in hind leg muscle thickness, the Veterinarian measured the thickness of thigh muscle in both legs using a digital caliper. There was no significant difference in muscle

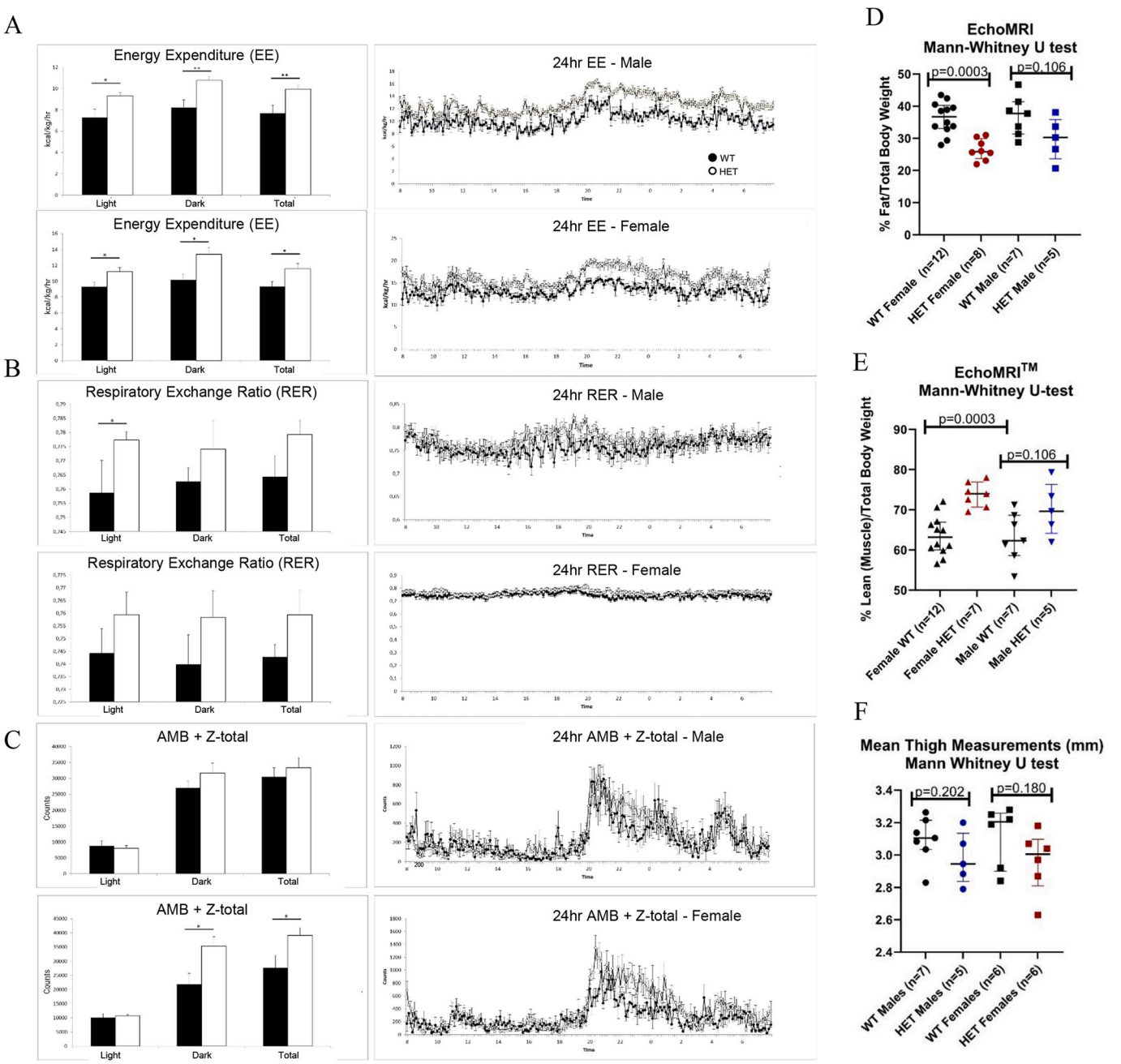

Fig. 4. Metabolic and EchoMRI™ analysis show differences in HET mice relative to WT littermates
A-C. Metabolic testing shows differences in energy expenditure, respiratory exchange ratio, and ambulation in WT (black bars) *versus* HET (white bars) mice at 7 months of age. Groups of adult male and female HET ($n = 5$/group) and WT (n = 3/group) mice were tested. (A) EE is significantly increased in both male and female HET mice, in both light and dark cycles. (B) There is a trend toward increased RER (VCO_2/O_2) in male and female HET mice. (C) Ambulation and rearing (AMB + Z total) are increased in female HET mice. Mann Whitney *U* test. Statistics were performed on days 3 to 5. The first 2 days are habituation and are not included in the analysis. D,E. EchoMRI™ analysis shows differences in HET mice relative to WT littermates. D, E. Female HET (red) mice have less body fat than WT (black) females; $p = 0.0003$, and male WT (black) *vs* HET (blue) are not different; $p = 0.106$. Statistical Analysis performed using the Mann Whitney U test two-tailed, median + interquartile range. F. No difference in the thickness of thigh muscle in male and female mice; $p > 0.05$. Mann Whitney U test, Median + Interquartile range. Male WT ($n = 7$), HET males (n = 5), WT females ($n = 6$) and HET females (n = 6) at 26–28 weeks of age were measured (mm) with digital calipers. (For interpretation of the references to colour in this figure legend, the reader is referred to the web version of this article.)

mass in the mice (Fig. 4F).

3.4. Neurobehavioral studies performed on HET and WT mice during early development did not identify significant deficits

Prior to weaning, pups were examined for developmental milestones that included surface righting, air righting, and cliff aversion (Hill et al., 2008). Beginning on postnatal day 7, a surface righting (SR) test was performed by placing a pup on their back on a plastic sheet and released. A time of two seconds or less is required for the pup to turn over with all four paws touching the surface. Both WT and HET pups were able to complete the test within the 2 s window (Supplemental Fig. 2). Air righting (AR) test was performed by placing pups upside down, approximately 10 cm above a cage containing bedding, and released. Landing on all four paws is required for successful completion of the test. WT and HET pups were able to successfully achieve this milestone.

During the cliff aversion (CA) test, a pup was positioned at the edge of a small plastic box with the digits of the forepaws and the snout overhanging. The time in seconds for the pup to turn and begin to crawl away from the edge is measured. A time of 30 s or less is required for successful completion of the test. HET and WT pups were able to successfully complete the test within the designated timeframe (Supplemental Fig. 2). The ledge test (Guyenet et al., 2010) showed that HET male and female mice can use their paws to successfully lower themselves into the cage without falling at postnatal ages. When WT and HET mice were examined from the rear, the mice walked normally on their paws, had no tremors, and did not have a drooping abdomen. None of the mice had kyphosis.

3.5. Neurobehavioral deficits of adult mice identify sensory and motor deficits

At P30, grip strength was measured by placing a mouse on the metal insert of their cage and once the insert was inverted timing their ability to hold with all four paws for 2 min. There was no difference in the grip of the male and female HET and WT mice (Fig. 5A).

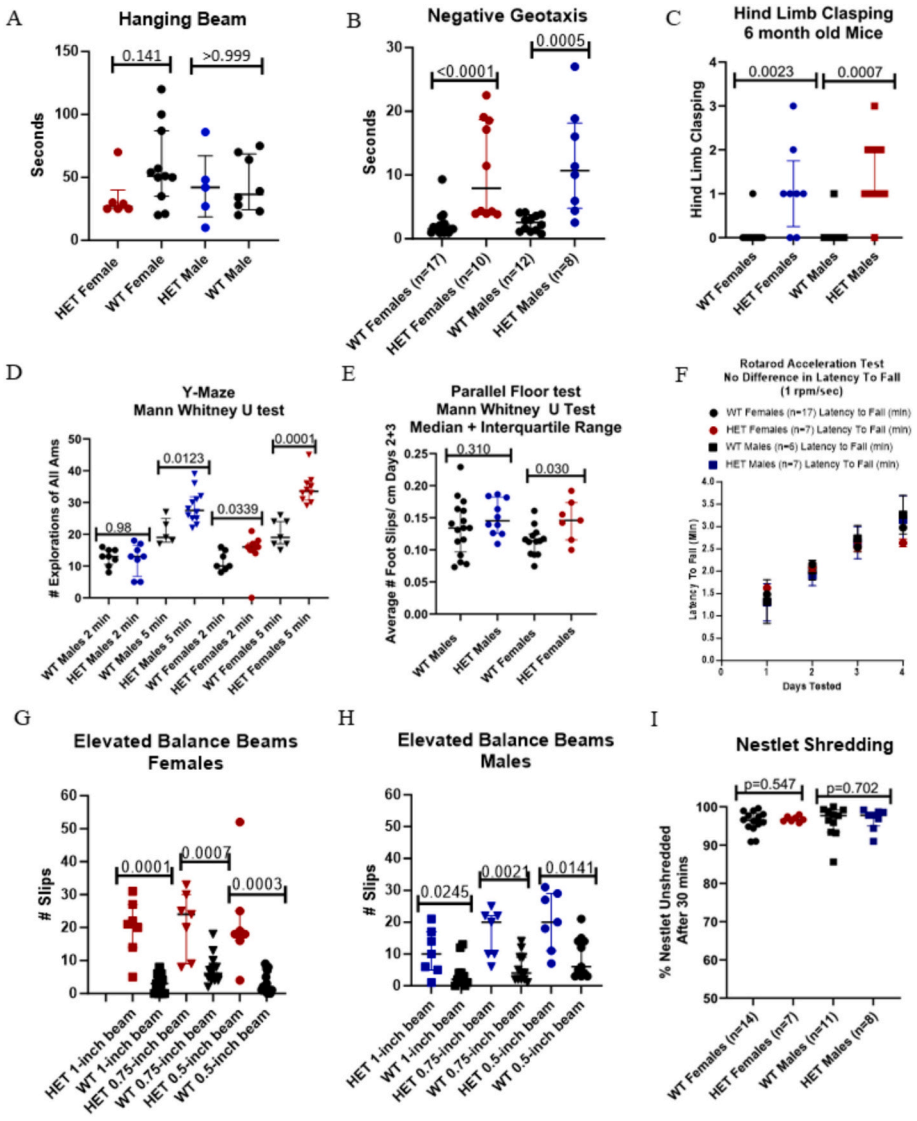

Fig. 5. Neurobehavioral testing shows that HET mice have deficits in sensory and motor coordination.
A. Grip strength of postnatal day 30 WT and HET mice are equivalent when assessed during an inverted hanging cage assay for 2 min; Mann Whitney U test. B. Altered proprioceptive behavior was identified in HET mice upon negative geotaxis testing. Negative geotaxis test shows HET mice, at postnatal day 45, take significantly longer to rotate head upward than WT. Female WT ($n = 17$; black) *vs* HET ($n = 10$; red); $p = 0.0001$; male WT ($n = 12$; black) *vs* HET ($n = 8$; blue), $p = 0.0005$. Statistical Analysis performed using the Mann Whitney U test two-tailed, median + interquartile range. C. Hindlimb clasping is present in male and female HET mice by 6 months of age. The severity is unaltered in HET mice over 1 year of age (not shown). WT ($n = 11$) and HET (n = 7) males, and WT ($n = 15$) and HET (n = 6) females were tested. Mann Whitney U test two-tailed, median + interquartile range. Females $p = 0.0007$; Males $p = 0.0023$. D. Exploration of all arms of a Y maze shows that male and female mice at 3 months of age spend more time exploring the arms than WT mice. Median + Interquartile range. Mann Whiney U test. E. Parallel floor testing measuring the average foot slip/cm on two consecutive days determined that only HET females (n = 7) perform worse than WT (n = 10) littermates; HET (n = 15) and WT (n = 10) males $p > 0.05$. Mann Whitney U test two-tailed, median + interquartile range. F. HET and WT mice show no difference in their latency to fall during accelerating rotarod testing. G,H. Elevated balance beam assays show adult female and male HET mice had significantly more slips when traversing three elevated balance beams of 0.5- (diamonds), 0.75-(squares), and 1-in. (circles) diameters than sex- and age-matched WT mice. G. Females and H. males mice traverse 1-in. beam (squares), 0.75-in. beam (inverted triangles), and 0.5-in. beam (circles). Median + Interquartile range. Mann Whiney U test. I. No difference in the % nestlet shredded in 30 min between HET and WT mice. Dried nestlet was weighed and quantified. (For interpretation of the references to colour in this figure legend, the reader is referred to the web version of this article.)

Negative geotaxis assays show that HET mice take longer to rotate head upward when placed on a vertical grid (Fig. 5B). The negative geotaxis assay is an unlearned automatic response to geogravitational stimuli. Motor and vestibular input is required for the mouse to recognize its orientation on a slope and turn around (Feather-Schussler and Ferguson, 2016). Mice prefer not to be placed head down and will rapidly rotate so they face upwards on a vertical grid. The assay can be used to assess sensorimotor ability and proprioceptive function, motor development (reflexes), activity and vestibular function. Young adult HET mice performed poorly on the negative geotaxis test taking significantly longer to rotate head upward on a vertical rack when compared with sex- and age-matched WT littermates suggestive of altered proprioceptive behavior.

HET mice develop hindlimb clasping (Zhu et al., 2016). When hindlimb clasping analysis was performed in 4–7 week old mice, neither HET nor WT mice exhibited hindlimb clasping. As the mice got older, we observed a difference in the hindlimb clasping in HET males but not females at 3–4 months of age (data not shown), and both males and females when tested at 6 months of age and older (Fig. 5C). The extent of hindlimb clasping severity in HET male and female mice at 1–1.5 years of age did not progress to all four paw clasping consistent with the DYNC1H1 mutation resulting in age-related loss of muscle tone and agile locomotor ability. Using a Y maze, male and female mice were allowed to freely explore all three arms for 5-min. Measures of the total number of times the mice entered any arm was recorded at 2- and 5-min. HET male and female mice entered all arms more times than WT mice indicative of increased locomotive activity (Fig. 5D). When mice were analyzed in the parallel floor chamber box and the number of slips relative to total movement were recorded there was no difference in the number of floor slips in male HET mice. Female HET mice had more slips relative to total movement than WT females. The data was averaged for days 2 and 3, with day 1 considered acclimation to the box (Fig. 5E). When mice were evaluated on an accelerating rotarod we observed no difference in endurance when the latency to fall was recorded (Fig. 5F). Elevated balance beam assays showed that both adult female and male HET mice had significantly more slips when traversing three different diameter elevated balance beams (0.5, 0.75 and 1 in.) than sex- and age-matched WT mice (Fig. 5G,H). When young adult male and female mice were tested for changes in nestlet shredding (Dorninger et al., 2020; Foltran et al., 2020; Angoa-Perez et al., 2013), there was no significant difference in the amount of nestlet shredded in WT and HET mice after 30 min (Fig. 1) indicating normal instincts in nest building. There was no difference in the number of marbles buried by WT and HET mice during the marble burying test (Jeyabalan et al., 2022) (data not shown) suggestive of normal compulsive behaviors. The combined neurobehavioral data strongly support motor deficits in HET mice.

3.6. *Abnormal lamination of the dorsal and lateral neocortex of HET mice*

Focal disruption of cortical laminar architecture has been observed in the cortex of children with autism (Pan et al., 2019), in Loa mice (Ori-McKenney and Vallee, 2011), and in mice with a cytoplasmic dynein mutation located within the microtubule binding domain (Romero et al., 2023). In order to assess the consequences of our patient-specific Dync1h1 mutation on forebrain development in more detail, we performed a histological survey of HET and WT brains using a number of different approaches. Paraffin and cryostat sections stained with H&E, Nissl, or propidium iodide (PI) all revealed normal cytoarchitecture of all subcortical structures evaluated in HET mice including the hippocampus, amygdala, thalamus, striatum, *etc.* (data not shown). Immunohistochemistry for myelinated fibers, showed normal development of all tracts and commissures. In contrast, all histological approaches consistently revealed disrupted neuronal lamination in the dorsal and lateral neocortex in 100% of HET male and female mice ($n > 10$ mice per sex). As shown in Fig. 6A, throughout the dorsal neocortex of HET mice, we observed a smearing of the border between layers I and II and a general increase in the H&E, Nissl, or PI-stained cells present in layer I compared to WT mice. In addition, even with basic histological stains there was preliminary indication that neurons in the HET layer 1 had inverted pyramidal morphologies relative to the pial surface. As shown in Fig. 6B, discrete heterotopia were also observed in layer I of the dorsal neocortex in HET mice which were characterized by focal accumulation of dozens-hundreds of cells tightly packed together. Finally, as shown in Fig. 6C, in the lateral cortex (down to the rhinal fissure), we saw a more intense cytoarchitecture defect in layer I of HET mice which was characterized by a saw-tooth pattern of cells in layer I (arrowhead).

As shown in Fig. 6D, we used MAP2 and NeuN immunostaining to characterize the cells in layer 1 of HET mice. In the HET cortex, we saw MAP2+ (magenta)/NeuN+ (green) neurons with pyramidal somata scattered throughout layer I including neurons demonstrating a loss of dendritic polarity relative to the pial surface. As shown in Fig. 6D (bottom row), MAP2+/NeuN+ neurons could be seen with apical dendrites pointing toward the white matter. Supplemental Fig. 3 shows quantification of increased MAP2+ inverted neurons in the dorsal cortex. Together these data indicate widespread cortical lamination defect in HET mice.

To further identify the population of affected neurons in layer I of HET mice, we used immunohistochemistry for upper and deep layer cortical neurons. First, as shown in Fig. 7A, we identified that smearing of the layer 1 border in HET mice was due to the presence of CUX1+ neurons normally present only in layer II-IV. We did not observe CTGF+ expressing neurons in layer I of HET mice in regions where layer I smearing was evident. However, focal heterotopia in the dorsal cortex contained diverse neurons from both upper and deeper layers. As shown in Fig. 7B, focal heterotopia were largely populated by CUX1+ neurons. However, we did observe heterotopia lacking substantial CUX1 + neurons (Fig. 7B) and we could also detect CTGF+ neurons in heterotopia which normally reside exclusively in layers V-VI. Finally, sections of the lateral cortex of HET mice revealed that the saw-tooth pattern of lamination defect was comprised entirely by CUX1+ neurons. Supplemental Fig. 4 shows increased number of CUX1+ cells in layer 1 of the neocortex of HET mice. These data indicate that while the general loss of the layer I border in the lateral and dorsal neocortex is due to CUX1+ neurons, focal heterotopia contain a more diverse and variable population of cells.

To characterize the morphology of neurons in greater detail, we crossed HET mice with Thy1-YFP mice (Feng et al., 2000) which express YFP throughout dendrites, soma, and axons in neocortical pyramidal cells of layers 2–6. Examination of Thy1-YFP/HET mice allowed for additional understanding of the lamination defects seen in the neocortex. First, in the dorsal cortex of HET brains where there was a smearing of the layer I and II borders, we observed YFP+ labeled neurons in layer I with a loss of dendritic polarity relative to the pial surface. As shown in Fig. 8A, these YFP+ neurons were inverted and had their apical dendrite pointing in the direction of the white matter, consistent with our observations of similar inverted MAP2+/NeuN+ neurons in HET cortex. Fig. 8Bshows that some but not all inverted YFP+ neurons were also Cux1+. Thy1-YFP/HET mice also allowed for further characterization of focal heterotopia in the dorsal cortex. Supplemental Fig. 5 shows the quantification of Thy1YFP+ cells in layer 1 of the dorsal cortex. As shown in Fig. 8C-D, YFP+ neurons were indeed found in focal heterotopia and some but not all were also labeled with CUX1 indicating that regions of heterotopia contain neurons from both upper layers (Cux1+) and deeper layers (YFP+/Cux1-). Finally, in the lateral cortex, we observed few YFP+ labeled neurons in areas containing the saw-tooth malformation. However, we observed bundling of YFP apical dendrites in areas between the saw-tooth pattern of cells in layer I (Fig. 8E). Taken together, our observations with Thy1YFP+/HET mice point to robust lamination defects in the neocortex of HET mice in both the dorsal and lateral neocortex.

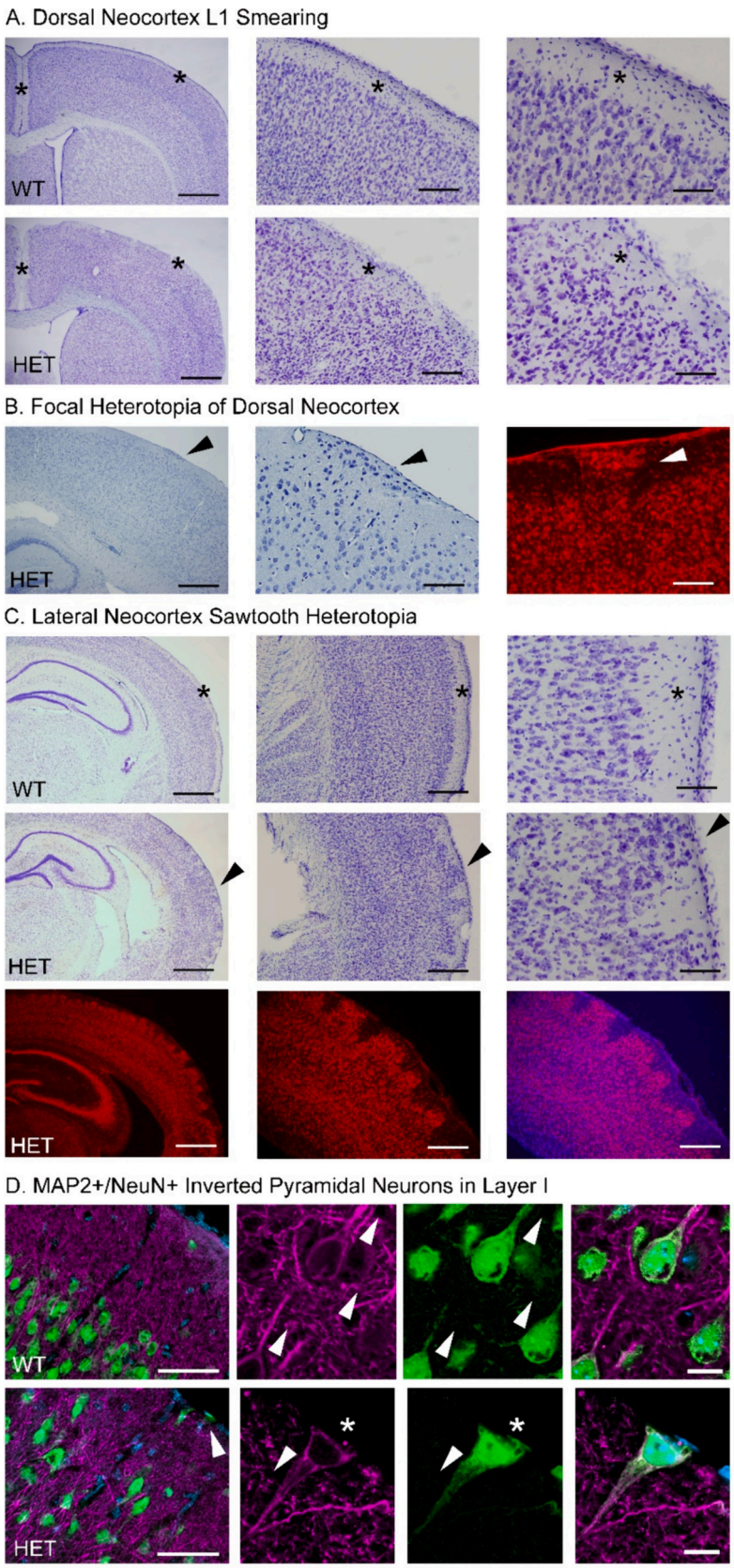

(caption on next page)

Fig. 6. Lamination defects of the dorsal and lateral neocortex of HET mice.
A. Nissl staining reveals normal border between layers I and II in WT mice (top row, asterisk) and smearing of layers I-II in HET mice (bottom row, asterisk). Left to right panels show increasing magnification of layers I-II. B. Examples of focal heterotopia consisting of an accumulation of Nissl- (left and middle panel) or propidium iodide- (right panel) stained cells in HET mice (arrowhead). Higher magnification of brain section in left panel is shown in middle panel. C. Normal cytoarchitecture of the lateral neocortex in WT mice (top panel, asterisk) and examples of sawtooth malformation in HET mice stained with Nissl (middle row, arrowhead) or PI (bottom row). D. Confocal microscopy shows examples of MAP2+/NeuN+ (magenta/green) neurons in layer II of the WT dorsal neocortex with apical dendrites pointing toward the pial surface (top row, arrowheads adjacent to the dendrites). Higher magnification of neurons in right panel shown in middle panels. Overlay with DAPI (blue) shown in right panel. Example of MAP2+/NeuN+ neuron in layer I and at the pial surface (arrowhead) with inverted apical dendrite in HET neocortex (asterisk). Higher magnification of neuron highlighted with arrowhead in right panel shown in middle panels. Overlay with DAPI (blue) shown in right panel denote pial surface. Scale bars (in microns) in A = 800 (left panels); 320 (middle panels); 160 (right panels); B = 320 (right panels); 160 (middle and left panels); C = 800 (left top panel); 320 (middle top panel); 160 (right top); 800 (left bottom panel); 300 (bottom middle panel); 300 (bottom right panel); D = 40 (left panels); 5 (all other panels). (For interpretation of the references to colour in this figure legend, the reader is referred to the web version of this article.)

4. Discussion

Cytoplasmic dynein 1 heavy chain, DYNC1H1, through its tail-like N-terminal, possess binding sites for different components of the dynein complex (both regulatory and structural) and for the different cargoes it transports. In addition, it is responsible for the contact and translocation of the dynein complex along microtubules through the large motor domain in its C-terminal. This motor domain forms a ring with six different ATPases (AAA1-AAA6), with AAA1, AAA3 and AAA4 able to hydrolyze ATP and use that energy for movement (Roossien et al., 2015).

While DYNC1H1 is found in all cells and has many housekeeping roles, it is crucial for normal nervous system function, where a single amino acid substitution can lead to neurological impairment (Hafezparast et al., 2003; Schiavo et al., 2013; Romero et al., 2023; Poirier et al., 2013; Amabile et al., 2020; Becker et al., 2020; Fiorillo et al., 2014). There are more than fourteen mutations reported in humans, mice, and zebrafish. All mutations identified to date are autosomal dominant with high penetrance (Schiavo et al., 2013). The importance of DYNC1H1's housekeeping function in all cells is likely why the majority of homozygous DYNC1H1 mutant mice do not survive birth. *De novo* single point mutations in DYNC1H1 have been reported at amino acids 92, 129, 317, 321, 387, 1567, 1962, 3336, 3344, 3384, and a *de novo* deletion was reported at 1659–1662, with various phenotypes and pathologies. Although clinical variants are present along the length of the protein, those associated with more severe CNS manifestations are mainly present in the motor domain. A mouse modeled after the human DYNC1H1 K3334N mutation located in the stalk (Romero et al., 2023) shares some similarities with the 3018S mutation including a reduction in body and brain weight, and abnormal neuronal migration in the cortex.

Our study is the first reported mouse model of a human *de novo* mutation within ATPase domain AAA4, a region close to the stalk and the microtubule-binding domain. There are currently four known human mutations in AAA4, located at N3014S, P3018S, E3048K and P3173R (Becker et al., 2020; Fiorillo et al., 2014). Alpha-fold (https://alphafold.ebi.ac.uk/) did not identify any alteration in the 3D structure when the ^{3018}proline was replaced by serine. Pondrfit predictions (pondr.com) for regions of disorder within the normal DYNC1H1 protein and the hydrophobic to hydrophilic P3018S HET region remain disordered and exposed for interactions (Fig. 9). The consensus amino acids surrounding the ATPase motif remain intact with no evidence for the mutation altering dynein's ATPase activity, ATP binding or hydrolysis. Walker (Walker et al., 1982) described a consensus motif associated with phosphate (P) binding (P-loop). The Walker motif or P-loop has two parts, Walker A and Walker B, with the Walker B motif 22 amino acids upstream of the Proline 3018 (green) and unchanged by the mutation. The **Walker A** motif, found in numerous ATP and GTP-using proteins, contains the consensus motif (G-(X)4-GK-[TS]), (Glycine-any four amino acids-Glycine-Lysine-[ThreonineSerine]), below in aqua. The conserved lysine is essential for nucleotide binding. In addition to this motif, there is an "LR nest" or cluster (in purple) and the motif xxGK (yellow). The hhhhDE **Walker B** motif, with h being any hydrophobic amino acid, D = aspartate and E = glutamate (highlighted in red), is located downstream of the Walker A motif (Hanson and Whiteheart, 2005). The aspartate and glutamate are important for ATP hydrolysis (Hanson and Whiteheart, 2005). Single-molecule fluorescence and optical tweezers studies determined that AAA1, AAA3, and AAA4 work together to regulate dynein function highlighting an essential role for AAA4 in dynein's stepping cycle and crosstalk among the motor's multiple AAA+ domains (Liu et al., 2020).

The Lissencephaly 1 protein (LIS1) binding site interacts with and regulates cytoplasmic dynein-1 by relieving dynein autoinhibition (Qiu et al., 2019; Marzo et al., 2020; Htet et al., 2020; Gillies et al., 2022; Elshenawy et al., 2020; Reimer et al., 2023). Mutations in LIS1 result in disruption of neurons in the cerebral cortex (Vallee et al., 2001) and several studies have examined the site of interaction between Lis1 and DYNC1H1 using yeast and human model systems (Gillies et al., 2022; Reimer et al., 2023; DeSantis et al., 2017). CryoEM demonstrated that in human dynein, regions E3196, Q3198, and N3202, are the regions that are required for disruption of Lis1 binding (Reimer et al., 2023). They note that only two known disease-related missense mutations in LIS1 are near a dynein binding site: both H277P, a lissencephaly mutation, and R342P, a double cortex syndrome mutation (Reimer et al., 2023).

In our study, a child with a heterozygous *de novo* point mutation at amino acid P3018S shares some phenotypes with other *de novo* point mutations including learning deficits associated with ASD, and mild motor deficits that still enable him to ski, but difficulty climbing and jumping. The child does not have seizures/epilepsy, microcephaly, or polymicrogyria. For his chronological age he is lean with little body fat. Based on our findings, the HET P3018S mutant mice are a good model for the motor deficits that were diagnosed in the child.

Metabolic and EchoMRI™ analyses were performed to address some of the observed differences in the HET P3018S mice. Metabolic testing shows HET mice expend more energy than WT mice suggesting increased locomotor activity. This is consistent of our finding using the Y maze. EchoMRI™ demonstrated that HET mice have lower fat and more lean muscle/total body weight than WT mice, which could be linked to their increased locomotion. When performing the parallel floor test the female HET, but not the HET males, performed significantly worse than age- and sex-matched control littermates. During Y-maze testing when mice freely explored all arms, male and female HET mice had increased movement in and out of all the arms after 5 mins. Although HET and control mice performed similarly during accelerated rotarod testing, HET mice performed significantly worse on the elevated balance beams and negative geotaxis testing, suggesting deficits in balance and proprioception.

Underlying mechanisms linking cytoplasmic dynein mutations to increased locomotion are not fully understood. Neurobehavioral studies indicate that disruptions in neuronal transport and signaling pathways contribute to changes in neuronal excitability, synaptic transmission, or circuitry in the brain, resulting in altered locomotor behavior. It is feasible that the abnormal neuronal migration in the cortex and ventricle enlargement contribute to altered circuitry and abnormal dendritic placement. HET mice at 8–9 weeks of age have smaller cerebrum than WT littermates, but mice at 10–12 months of age do not show

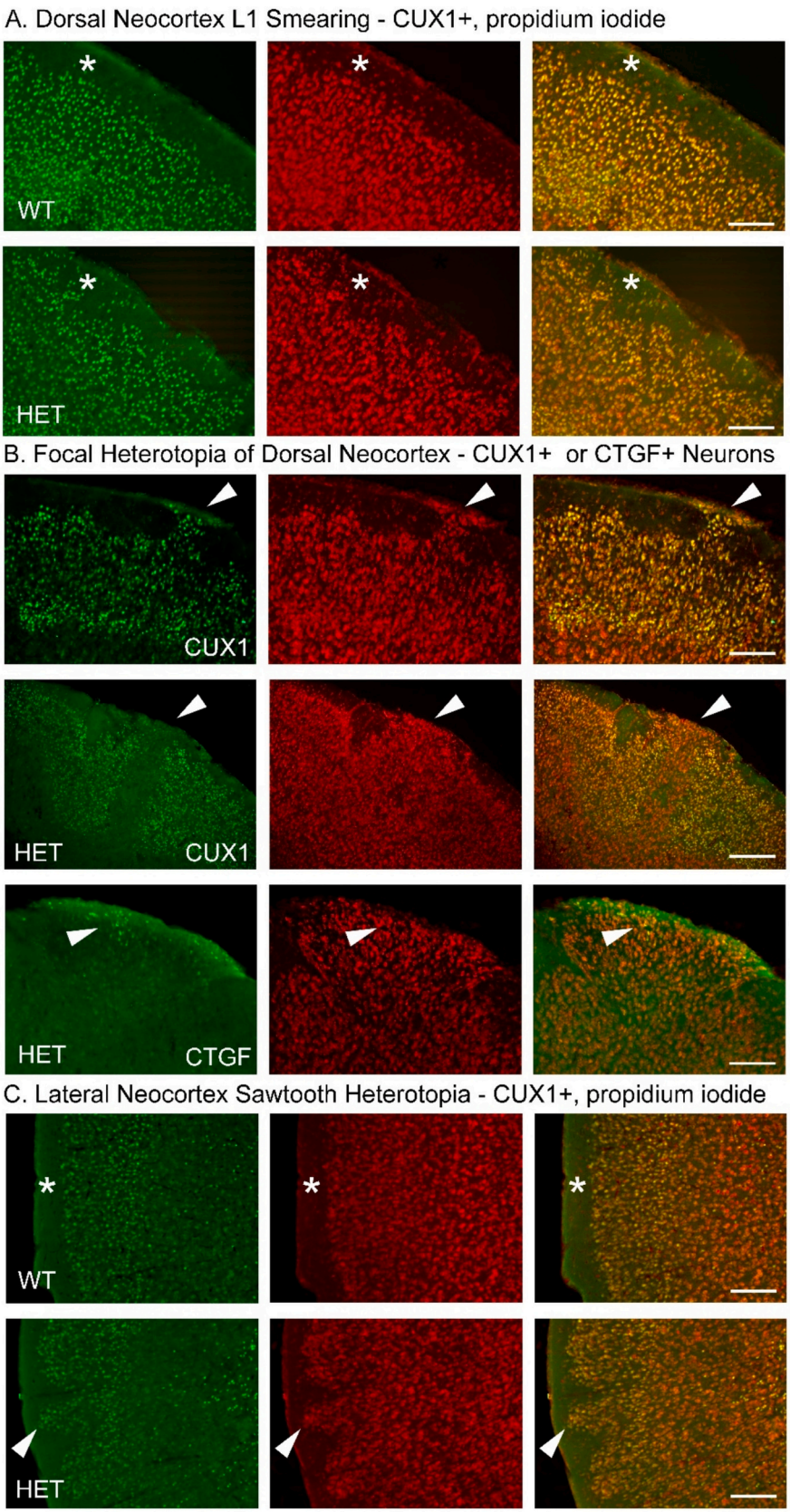

(caption on next page)

Fig. 7. Lamination defects of the dorsal and lateral neocortex of HET mice.
A. CUX1 (green) and propidium iodide (red) staining reveals normal border between layers I and II (asterisk) in WT mice (top row) and smearing of layers I-II in HET mice (bottom row). Right panels show overlay of staining. B. Examples of focal heterotopia in HET mice consisting of an accumulation of CUX1+ (green) neurons (top row) or with sparse CUX1+ neurons (middle row). Example of heterotopia in HET neocortex with deep layer CTGF+ (green) neurons (bottom panel). Propidium iodide counterstaining and overly images shown in middle and right panel, respectively. Higher magnification of brain section in left panel is shown in middle panel. C. CUX1+ (green) and propidium iodide (red) staining of the normal cytoarchitecture of the lateral neocortex in WT mice (top panel) with no CUX1+ neurons in layer 1 (asterisk), and sawtooth malformation in HET mice (bottom row, arrowhead). All scale bars = 100 μm. (For interpretation of the references to colour in this figure legend, the reader is referred to the web version of this article.)

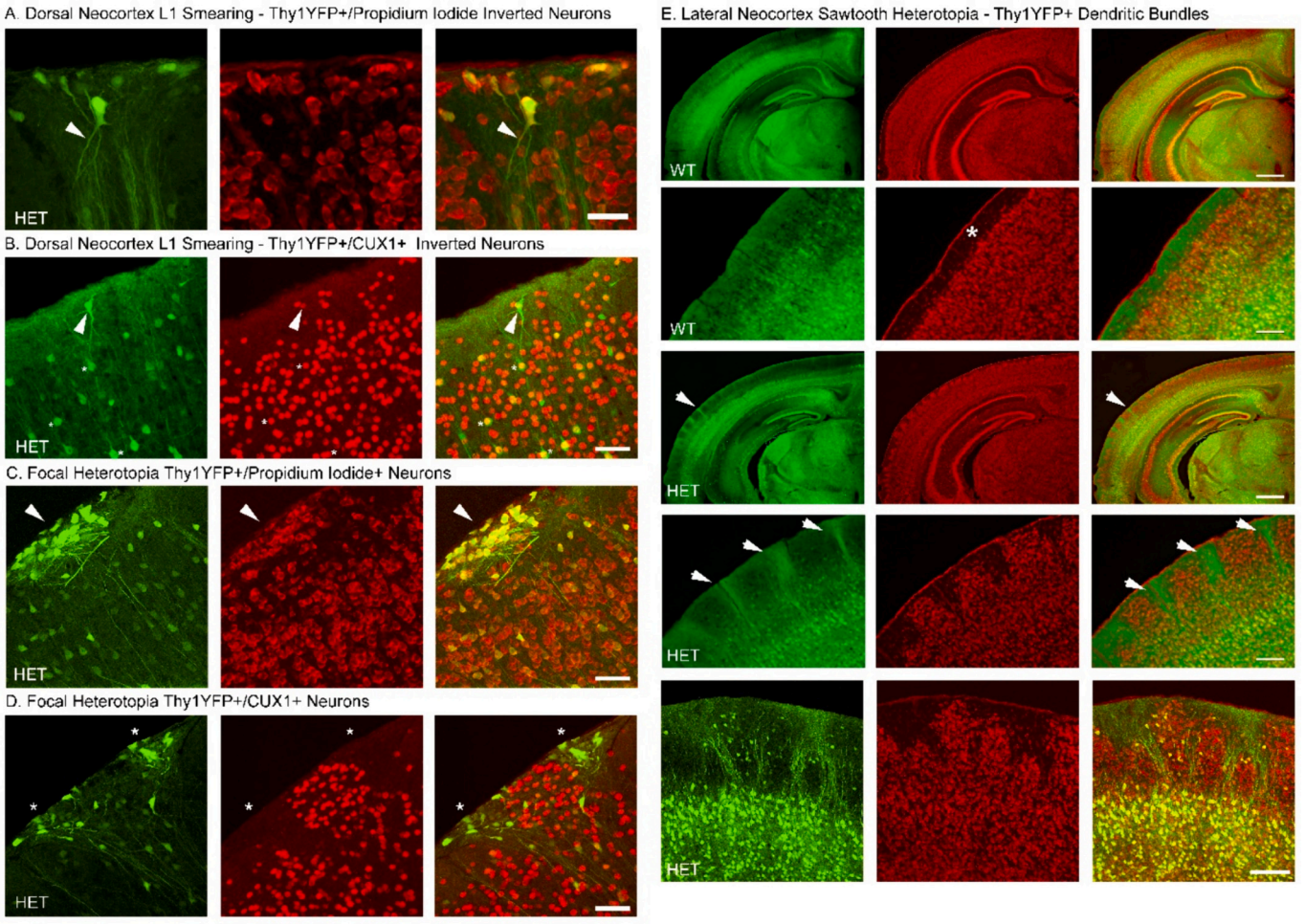

Fig. 8. Lamination defects of the dorsal and lateral neocortex of Thy1YFP+/HET mice.
A. YFP+ (green) neuron in layer I of HET cortex with inverted pyramidal cell morphology (arrowhead). PI counterstaining and overlay or images shown in middle and right panels, respectively. B. YFP+/CUX1+ (green/red) neuron in layer I of HET cortex with inverted pyramidal cell morphology(arrowhead). C. Focal accumulation of YFP+ (green) neurons in heterotopia in HET cortex (arrowhead). PI counterstaining and overlay or images shown in middle and right panels, respectively. D. YFP+ neurons are interspersed with CUX1+ (red) neurons in focal heterotopia of HET mice. Overlay of images shown in right panel. E. YFP+ (green) and propidium iodide (red) staining of the normal cytoarchitecture of the lateral neocortex in WT mice (top 2 rows; arrowhead denotes layer 1) and sawtooth malformation in HET mice (bottom 3 rows). Bundling of YFP+ dendrites (arrowhead) visible in between accumulation of PI labeled cell bodies in layer I. Scale bars (in microns) in A = 30; B-D = 150; E = 600 (top and 3rd row); 200 last row. (For interpretation of the references to colour in this figure legend, the reader is referred to the web version of this article.)

the same deficits. Meta-analyses of MRI, and postmortem human brain analyses showed that overall brain size was near the normal average in both adolescent and adults on the autism spectrum, with differences from normal being only about 1% in volume or weight. Enlarged ventricles are observed in both antenatal and postnatal subjects with ASD, independent from total brain volume. In antenatal subjects, enlarged ventricles are a marker of altered cortical development with implications for later cognitive and behavioral outcomes. MicroCT was able to identify enlargement of the ventricular system in our mouse model.

Fine motor impairment observed in HET mice upon balance beam testing likely correlates with cortical heterotopia (Fox and Walsh, 1999). The cerebral cortex mediates higher-order cognitive processing, learning, and memory. These functions are due to interactions between the different cell populations in the cortex (Chu and Anderson, 2015). Newborn neurons progressively migrate along radial glia fibers (Rakic, 2003) up to the cortical plate, where they give rise to the different layers of the cortex (layers 1–6) in an inward to outward order. The first postmitotic neurons generated occupy the most distal layers, and the last ones generated migrate up toward the pial surface. Neuronal migration can be hindered by altered intracellular transport, including the movement of organelles, cellular components and signaling molecules. Impairment of dynein can disrupt the transport of essential molecules

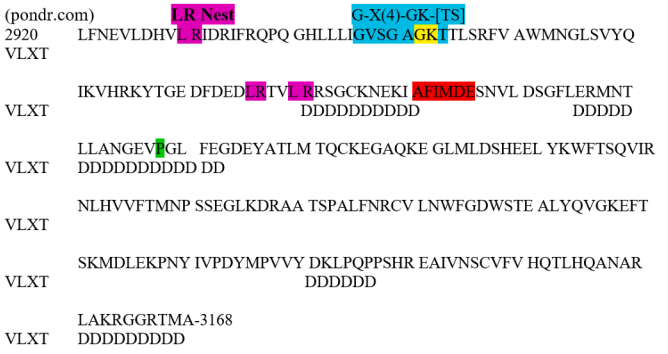

Fig. 9. Walker Sequences Upstream of the *De Novo* Dync1h1 P3018S Mutation Is Intact and Regions of Disorder Within the protein region (pndr.com) are unchanged.
Shown is amino acids 2920–3168 spanning a large region of the carboxy region of DYNC1H1. The proline (P) mutated to Serine at amino acid 3018 is shown in green. Walker Motif consists of Walker A and B. **Walker A Motif**: Glycine-any four amino acids-Glycine-Lysine-[ThreonineSerine] (G-X(4)-GK-[TS]) is highlighted in aqua. The conserved lysine is essential for nucleotide binding. The motif also includes the "LR nest" or cluster (in purple) and the motif xxGK (yellow). **Walker B Motif**: The hhhhDE Walker B motif, with h being any hydrophobic amino acid, D = aspartate and E = glutamate (highlighted in red), is located downstream of the Walker A motif (Hanson and Whiteheart, 2005). The aspartate and glutamate are important for ATP hydrolysis (Hanson and Whiteheart, 2005). (For interpretation of the references to colour in this figure legend, the reader is referred to the web version of this article.)

within migrating cells, affecting their ability to respond to guidance cues and to navigate along their migration path.

Cortical projection neurons (CPNs) in different layers have different functions and express layer specific genes, including transcription factors (TFs) that function in CPN specification and differentiation. The transcription factor cux-like homebox-1 (CUX1) is enriched in post-mitotic neurons within layers 2–4, playing important roles in their dendritic arborization and synapse formation. CTGF is enriched in layers 5 and 6 and is involved in specification, maintenance, and/or connectivity of neuronal populations in the nervous system (Hoerder-Suabedissen and Molnar, 2013). These CPNs have a distinct morphology, projecting their dendrites toward the pial surface of the brain. The correct development of the neocortex requires an adequate migration of neurons into their appropriate positions and the acquisition of layer-specific identities. The P3018S HET mice have errors in migration with neurons migrating into layer 1 of the cortex and extending to the pial surface. The large extent of the neocortex is affected in HET mice including the dorsal and lateral cortices. Multiple antibody markers demonstrated that these abnormal neurons originated from deeper cortical layers. The shape of the NeuN+ neurons within layer 1 are not round as predicted for interneurons. They are pyramidal shaped and are positive for CUX1 and connective tissue growth factor (CTGF) (Friedrichsen et al., 2003; Heuer et al., 2003), transcription factors associated with neurons in layer II/III and VI, respectively. Additionally, SMI32, an antibody to middle and high neurofilament proteins expressed in layer III and V pyramidal neurons, identified mis-localized neurons in layer I.

In some individuals with intellectual disability and *DYNC1H1* gene mutations, brain malformation with many small folds called polymicrogyria are reported (Vallee et al., 2001). Although rodent brains do not have sulci or gyri, we observed unusual bumps on the surface of the cerebrum in ~67% of HET mice examined, along with the abnormal migration of neurons within layer I of the cortex expressing CUX1 and CTGF.

We determined that HET mice have hindlimb clasping at 6 months of age but the extent of clasping did not progress and no loss of motor neurons were observed following immunostaining with SMI32, MAP2 or NeuN. DYNC1H1 CraY1055C mutant mice show hindlimb clasping because of a defect in sensory neuron function (Dupuis et al., 2009). Cra mice also have proprioceptive neuropathy, enlarged ventricles, and striatal atrophy (Braunstein et al., 2010).

NeuN/Fox3 is a neuronal nuclear protein considered a marker of neuron differentiation, and used to identify postmitotic neurons (Gusel'nikova and Korzhevskiy, 2015). NeuN immunofluorescent staining identified abnormal neuronal migration into layer 1 of the cortex of P3018S HET mice. Immunostaining with layers 2–3 neuronal marker Cux1, and PI, shows patched disruption of cortical laminar architecture, Cux1+ neurons in layer 1, and incorrect dendritic orientation in some neurons in layer 1/2 of HET male and female mice. Layer formation dysregulation and altered migration is reported in humans with the DYNC1H1 mutation K3334N (Romero et al., 2023) and in ASD. Dynein is important for the organization and stabilization of microtubules, which are essential components of the cell's cytoskeleton. Impaired dynein function can result in abnormal microtubule organization, affecting the integrity and guidance of neuronal cell migration. Without proper microtubule organization, the structural support necessary for directed migration may be compromised.

In vitro, neurons from Sprawling mice had shortened MAP2+ dendritic arborizations with no neuronal loss (Tynan et al., 2000). MAP2, is the major MAP in post-mitotic neurons. Both MAP2 (~250 kDa) and the dynein-dynactin complex (~1.4 MDa) are bulky proteins. *In vitro* studies demonstrate that active transport by cytoplasmic dynein maintains localization of MAP2 in dendrites in developing neurons (Yonemura et al., 2023). We observe correct localization of MAP2 in cortical and cerebella dendrites. Using MAP2 immunostaining we found aberrantly oriented neurons with MAP2+ orientation of dendrites facing away from the pial surface suggesting that the P3018S HET mutation does not alter MAP2 dynein interactions but does impact dendritic orientation.

In conclusion, our results add to the noted syndrome of pathological mutations in DYNC1H1 and reinforce the role of cytoplasmic dynein in disorders of neuronal migration highlighting structural and neurobehavioral deficits.

Author contribution

Raddy Ramos sectioned brains, performed immunofluorescent staining and confocal microscopy, performed MicroCT, prepared composite figures, wrote portions of the manuscript, and was instrumental in generating the data for Figs. 6–8.

Maider Michelena Beltran De Heredia performed immunofluorescent staining and microscopy, performed behavioral studies including the parallel floor plate assays, analyzed data and wrote portions of the Methods sections.

Yongwei Zhang generated the cytoplasmic dynein heterozygous P3018S knockin mice and performed the genotyping (fee for service).

Randy Stout performed confocal microscopy and helped generate composite figures.

Jaafar Tindi demonstrated the parallel floor plate assay and helped with its statistical analysis.

Liching Wu and Gary J. Schwartz provided expertise for the Metabolic Chamber, and performed the statistical analysis for Fig. 4.

Yair M. Botbol performed western blot analysis and generated the figures quantifying dynein, myelin basic protein (MBP), actin, and vinculin in brain homogenates.

Ankita Poojari purified the proteins from the dissected brain regions.

Simone Sidoli purified the proteins from the dissected brain regions, performed the nanoLC-MS/MS, and analyzed the data sets.

Tammy Rakowski-Anderson oversees the Veterinary care for the mice and measured thigh muscle thickness of wildtype and HET mice.

Bridget Shafit-Zagardo initiated the project, saw to the generation of the Dync1h1 P3018S strain and all subsequent strains used in the study, maintained the colonies, performed necropsies, perfused mice, performed immunofluorescent staining and light microscopy, behavioral

studies, prepared composite figures, and with Dr. Ramos wrote the manuscript.

CRediT authorship contribution statement

Raddy L. Ramos: Writing – review & editing, Writing – original draft, Methodology, Formal analysis, Data curation, Conceptualization. **Maider Michelena Beltran De Heredia:** Methodology, Investigation, Formal analysis, Data curation. **Yongwei Zhang:** Methodology, Investigation. **Randy F. Stout:** Methodology, Formal analysis, Conceptualization. **Jaafar O. Tindi:** Investigation, Formal analysis. **Liching Wu:** Methodology, Investigation, Formal analysis. **Gary J. Schwartz:** Investigation, Formal analysis. **Yair M. Botbol:** Methodology, Investigation, Formal analysis. **Simone Sidoli:** Validation, Supervision, Software, Resources, Methodology, Formal analysis, Data curation. **Ankita Poojari:** Methodology, Data curation. **Tammy Rakowski-Anderson:** Methodology, Investigation. **Bridget Shafit-Zagardo:** Writing – review & editing, Writing – original draft, Supervision, Resources, Project administration, Methodology, Investigation, Formal analysis, Data curation, Conceptualization.

Declaration of competing interest

The authors declare no conflicts of interest. All the animals were bred, and maintained in the Barrier Facility under the guidance of the Albert Einstein College of Medicine (AECOM) veterinary staff and Dr. Shafit-Zagardo's approved protocol number 00001158. All procedures are in complete compliance with the AECOM Institutional Review Board and NIH Guide for the Care of Laboratory Animals. The mice were continually monitored for any distress including changes in excretion, or lethargy.

Data availability

Mice will be available to the Scientific Community through the PI.

Acknowledgements

Funding for the study was provided by the Rose F. Kennedy Center for Intellectual Disorders and Developmental Disabilities (IDDRC) program funded by NIH grant 1 P50 HD105352 and The Gottbetter Fund (BSZ). Metabolic and EcoMRI analyses were funded by the Einstein-Mount Sinai Diabetes Research Center Animal Physiology Core P30 DK020541. Balance beam and y-maze testing was supported by an NIA Nathan Shock Center Aging grant P30AG038072. The Sidoli lab gratefully acknowledges funding from the Hevolution Foundation (AFAR), the Einstein-Mount Sinai Diabetes Center, and the NIH Office of the Director (S10OD030286). We thank the NYIT Imaging Center for use of the confocal microscope and software and the NYIT College of Osteopathic Medicine Visualization Center for MicroCT scanning (NSF 1828305). The Analytic Imaging Facility, Albert Einstein College of Medicine, is supported by an NCI Cancer Center support grant P30CA013330. The 3DHistec Panoramic 250 Flash III P250 slide scanner is supported by SIG#1S10OD019961–01. We thank Dr. Yongtai Lo, Professor, Department of Epidemiology and Population Health for advice on statistical analyses. We thank Ms. Hillary Guzik for help with some of the images and scanning slides. We thank Dr. Kai Wu for help with the balance beam assay, and helpful discussions. We thank Ms. Bhati Chavda and Dr. Rabia Khawaja for advising us on the y-maze test. We thank Dr. Shun Mei Liu for teaching us how to perform EchoMRI™. We thank Dr. Streamson Chua for helpful discussions on metabolism and Dr. Maria Gulinello for advice on behavioral studies.

Appendix A. Supplementary data

Supplementary data to this article can be found online at https://doi.org/10.1016/j.nbd.2024.106594.

References

Amabile, S., Jeffries, L., McGrath, J.M., et al., 2020. DYNC1H1-related disorders: a description of four new unrelated patients and a comprehensive review of previously reported variants. Am. J. Med. Genet. A 182 (9), 2049–2057. https://doi.org/10.1002/ajmg.a.61729. Sep.

Angoa-Perez, M., Kane, M.J., Briggs, D.I., Francescutti, D.M., Kuhn, D.M., 2013. Marble burying and nestlet shredding as tests of repetitive, compulsive-like behaviors in mice. J. Vis. Exp. (82), 50978. https://doi.org/10.3791/50978. Dec 24.

Asante, D., Stevenson, N.L., Stephens, D.J., 2014. Subunit composition of the human cytoplasmic dynein-2 complex. J. Cell Sci. 127 (Pt 21), 4774–4787. https://doi.org/10.1242/jcs.159038. Nov 1.

Banks, G.T., Fisher, E.M., 2008. Cytoplasmic dynein could be key to understanding neurodegeneration. Genome Biol. 9 (3), 214. https://doi.org/10.1186/gb-2008-9-3-214.

Becker, L.L., Dafsari, H.S., Schallner, J., et al., 2020. The clinical-phenotype continuum in DYNC1H1-related disorders-genomic profiling and proposal for a novel classification. J. Hum. Genet. 65 (11), 1003–1017. https://doi.org/10.1038/s10038-020-0803-1. Nov.

Braunstein, K.E., Eschbach, J., Rona-Voros, K., et al., 2010. A point mutation in the dynein heavy chain gene leads to striatal atrophy and compromises neurite outgrowth of striatal neurons. Hum. Mol. Genet. 19 (22), 4385–4398. https://doi.org/10.1093/hmg/ddq361. Nov 15.

Chen, X.J., Levedakou, E.N., Millen, K.J., Wollmann, R.L., Soliven, B., Popko, B., 2007. Proprioceptive sensory neuropathy in mice with a mutation in the cytoplasmic dynein heavy chain 1 gene. J. Neurosci. 27 (52), 14515–14524. https://doi.org/10.1523/JNEUROSCI.4338-07.2007. Dec 26.

Chu, J., Anderson, S.A., 2015. Development of cortical interneurons. Neuropsychopharmacology 40 (1), 16–23. https://doi.org/10.1038/npp.2014.171. Jan.

de Ligt, J., Willemsen, M.H., van Bon, B.W., et al., 2012. Diagnostic exome sequencing in persons with severe intellectual disability. N. Engl. J. Med. 367 (20), 1921–1929. https://doi.org/10.1056/NEJMoa1206524. Nov 15.

DeSantis, M.E., Cianfrocco, M.A., Htet, Z.M., Tran, P.T., Reck-Peterson, S.L., Leschziner, A.E., 2017. Lis1 has two opposing modes of regulating cytoplasmic dynein. Cell 170 (6), 1197–1208 e12. https://doi.org/10.1016/j.cell.2017.08.037. Sep 7.

Dorninger, F., Zeitler, G., Berger, J., 2020. Nestlet shredding and nest building tests to assess features of psychiatric disorders in mice. Bio-Protoc. 10 (24) https://doi.org/10.21769/BioProtoc.3863. Dec 20.

Driskell, O.J., Mironov, A., Allan, V.J., Woodman, P.G., 2007. Dynein is required for receptor sorting and the morphogenesis of early endosomes. Nat. Cell Biol. 9 (1), 113–120. https://doi.org/10.1038/ncb1525. Jan.

Duchen, L.W., 1974. A dominant hereditary sensory disorder in the mouse with deficiency of muscle spindles: the mutant sprawling. J. Physiol. 237 (2), 10P–11P. Mar.

Dupuis, L., Fergani, A., Braunstein, K.E., et al., 2009. Mice with a mutation in the dynein heavy chain 1 gene display sensory neuropathy but lack motor neuron disease. Exp. Neurol. 215 (1), 146–152. https://doi.org/10.1016/j.expneurol.2008.09.019. Jan.

Elshenawy, M.M., Kusakci, E., Volz, S., Baumbach, J., Bullock, S.L., Yildiz, A., 2020. Lis1 activates dynein motility by modulating its pairing with dynactin. Nat. Cell Biol. 22 (5), 570–578. https://doi.org/10.1038/s41556-020-0501-4. May.

Feather-Schussler, D.N., Ferguson, T.S., 2016. A battery of motor tests in a neonatal mouse model of cerebral palsy. J. Vis. Exp. (117) https://doi.org/10.3791/53569. Nov 3.

Feng, G., Mellor, R.H., Bernstein, M., et al., 2000. Imaging neuronal subsets in transgenic mice expressing multiple spectral variants of GFP. Neuron 28 (1), 41–51. https://doi.org/10.1016/s0896-6273(00)00084-2. Oct.

Fiorillo, C., Moro, F., Yi, J., et al., 2014. Novel dynein DYNC1H1 neck and motor domain mutations link distal spinal muscular atrophy and abnormal cortical development. Hum. Mutat. 35 (3), 298–302. https://doi.org/10.1002/humu.22491. Mar.

Foltran, R.B., Stefani, K.M., Hocht, C., Diaz, S.L., 2020. Neurochemical, behavioral, and neurogenic validation of a hyposerotonergic animal model by voluntary oral consumption of para-chlorophenylalanine. ACS Chem. Neurosci. 11 (6), 952–959. https://doi.org/10.1021/acschemneuro.9b00687. Mar 18.

Fox, J.W., Walsh, C.A., 1999. Periventricular heterotopia and the genetics of neuronal migration in the cerebral cortex. Am. J. Hum. Genet. 65 (1), 19–24. https://doi.org/10.1086/302474. Jul.

Friedrichsen, S., Heuer, H., Christ, S., et al., 2003. CTGF expression during mouse embryonic development. Cell Tissue Res. 312 (2), 175–188. https://doi.org/10.1007/s00441-003-0712-6. May.

Gibson-Corley, K.N., Olivier, A.K., Meyerholz, D.K., 2013. Principles for valid histopathologic scoring in research. Vet. Pathol. 50 (6), 1007–1015. https://doi.org/10.1177/0300985813485099. Nov.

Gillies, J.P., Reimer, J.M., Karasmanis, E.P., et al., 2022. Structural basis for cytoplasmic dynein-1 regulation by Lis1. Elife 11. https://doi.org/10.7554/eLife.71229. Jan 7.

Gross, S.P., Welte, M.A., Block, S.M., Wieschaus, E.F., 2000. Dynein-mediated cargo transport in vivo. A switch controls travel distance. J. Cell Biol. 148 (5), 945–956. https://doi.org/10.1083/jcb.148.5.945. Mar 6.

Gruber, R.C., Ray, A.K., Johndrow, C.T., et al., 2014. Targeted GAS6 delivery to the CNS protects axons from damage during experimental autoimmune encephalomyelitis. J. Neurosci. 34 (49), 16320–16335. https://doi.org/10.1523/jneurosci.2449-14.2014. Dec 03.

Gusel'nikova, V.V., Korzhevskiy, D.E., 2015. NeuN as a neuronal nuclear antigen and neuron differentiation marker. Acta Nat. 7 (2), 42–47. Apr-Jun.
Guyenet, S.J., Furrer, S.A., Damian, V.M., Baughan, T.D., La Spada, A.R., Garden, G.A., 2010. A simple composite phenotype scoring system for evaluating mouse models of cerebellar ataxia. J. Vis. Exp. (39) https://doi.org/10.3791/1787. May 21.
Habura, A., Tikhonenko, I., Chisholm, R.L., Koonce, M.P., 1999. Interaction mapping of a dynein heavy chain. Identification of dimerization and intermediate-chain binding domains. J. Biol. Chem. 274 (22), 15447–15453. https://doi.org/10.1074/jbc.274.22.15447. May 28.
Hafezparast, M., Klocke, R., Ruhrberg, C., et al., 2003. Mutations in dynein link motor neuron degeneration to defects in retrograde transport. Science 300 (5620), 808–812. https://doi.org/10.1126/science.1083129. May 2.
Hanson, P.I., Whiteheart, S.W., 2005. AAA+ proteins: have engine, will work. Nat. Rev. Mol. Cell Biol. 6 (7), 519–529. https://doi.org/10.1038/nrm1684. Jul.
Harms, M.B., Ori-McKenney, K.M., Scoto, M., et al., 2012. Mutations in the tail domain of DYNC1H1 cause dominant spinal muscular atrophy. Neurology 78 (22), 1714–1720. https://doi.org/10.1212/WNL.0b013e3182556c05. May 29.
Harrison, L., Pfuhlmann, K., Schriever, S.C., Pfluger, P.T., 2019. Profound weight loss induces reactive astrogliosis in the arcuate nucleus of obese mice. Mol. Metab. 24, 149–155. https://doi.org/10.1016/j.molmet.2019.03.009. Jun.
Heuer, H., Christ, S., Friedrichsen, S., et al., 2003. Connective tissue growth factor: a novel marker of layer VII neurons in the rat cerebral cortex. Neuroscience 119 (1), 43–52. https://doi.org/10.1016/s0306-4522(03)00100-3.
Hill, J.M., Lim, M.A., Stone, M.M., 2008. Developmental milestones in the newborn mouse. In: Gozes, I. (Ed.), Neuropeptide Techniques. Humana Press, pp. 131–149.
Hoang, H.T., Schlager, M.A., Carter, A.P., Bullock, S.L., 2017. DYNC1H1 mutations associated with neurological diseases compromise processivity of dynein-dynactin-cargo adaptor complexes. Proc. Natl. Acad. Sci. USA 114 (9). https://doi.org/10.1073/pnas.1620141114. Feb 28. E1597-E1606.
Hoerder-Suabedissen, A., Molnar, Z., 2013. Molecular diversity of early-born subplate neurons. Cereb. Cortex 23 (6), 1473–1483. https://doi.org/10.1093/cercor/bhs137. Jun.
Htet, Z.M., Gillies, J.P., Baker, R.W., Leschziner, A.E., DeSantis, M.E., Reck-Peterson, S. L., 2020. LIS1 promotes the formation of activated cytoplasmic dynein-1 complexes. Nat. Cell Biol. 22 (5), 518–525. https://doi.org/10.1038/s41556-020-0506-z. May.
Insinna, C., Baye, L.M., Amsterdam, A., Besharse, J.C., Link, B.A., 2010. Analysis of a zebrafish dync1h1 mutant reveals multiple functions for cytoplasmic dynein 1 during retinal photoreceptor development. Neural Dev. 5 (12) https://doi.org/10.1186/1749-8104-5-12. Apr 22.
Jeyabalan, S., Bala, L., Subramanian, K., et al., 2022. Potential effects of noni (Morinda citrifolia L.) fruits extract against obsessive-compulsive disorder in marble burying and nestlet shredding behavior mice models. Front. Pharmacol. 13, 993927 https://doi.org/10.3389/fphar.2022.993927.
Jordens, I., Fernandez-Borja, M., Marsman, M., et al., 2001. The Rab7 effector protein RILP controls lysosomal transport by inducing the recruitment of dynein-dynactin motors. Curr. Biol. 11 (21), 1680–1685. https://doi.org/10.1016/s0960-9822(01)00531-0. Oct 30.
Kamens, H.M., Crabbe, J.C., 2007. The parallel rod floor test: a measure of ataxia in mice. Nat. Protoc. 2 (2), 277–281. https://doi.org/10.1038/nprot.2007.19.
Kastner, D.B., Kharazia, V., Nevers, R., et al., 2020. Scalable method for micro-CT analysis enables large scale quantitative characterization of brain lesions and implants. Sci. Rep. 10 (1), 20851. https://doi.org/10.1038/s41598-020-77796-3. Nov 30.
Kural, C., Kim, H., Syed, S., Goshima, G., Gelfand, V.I., Selvin, P.R., 2005. Kinesin and dynein move a peroxisome in vivo: a tug-of-war or coordinated movement? Science 308 (5727), 1469–1472. https://doi.org/10.1126/science.1108408. Jun 3.
Langworthy, M.M., Appel, B., 2012. Schwann cell myelination requires dynein function. Neural Dev. 7, 37. https://doi.org/10.1186/1749-8104-7-37. Nov 20.
Li, J.T., Dong, S.Q., Zhu, D.Q., et al., 2022. Expanding the phenotypic and genetic spectrum of neuromuscular diseases caused by DYNC1H1 mutations. Front. Neurol. 13, 943324 https://doi.org/10.3389/fneur.2022.943324.
Lipka, J., Kuijpers, M., Jaworski, J., Hoogenraad, C.C., 2013. Mutations in cytoplasmic dynein and its regulators cause malformations of cortical development and neurodegenerative diseases. Biochem. Soc. Trans. 41 (6), 1605–1612. https://doi.org/10.1042/BST20130188. Dec.
Liu, X., Rao, L., Gennerich, A., 2020. The regulatory function of the AAA4 ATPase domain of cytoplasmic dynein. Nat. Commun. 11 (1), 5952. https://doi.org/10.1038/s41467-020-19477-3. Nov 23.
Marzo, M.G., Griswold, J.M., Markus, S.M., 2020. Pac1/LIS1 stabilizes an uninhibited conformation of dynein to coordinate its localization and activity. Nat. Cell Biol. 22 (5), 559–569. https://doi.org/10.1038/s41556-020-0492-1. May.
Mayoral-Palarz, K., Neves-Carvalho, A., Duarte-Silva, S., Monteiro-Fernandes, D., Maciel, P., Khodakhah, K., 2022. Cerebellar neuronal dysfunction accompanies early motor symptoms in spinocerebellar ataxia type 3. Dis. Model. Mech. 15 (8). Aug 1. https://doi.org/10.1242/dmm.049514.
Moller, B., Coppola, A., Jungbluth, H., Dafsari, H.S., 1993. DYNC1H1-related disorders. In: Adam, M.P., Feldman, J., Mirzaa, G.M., et al. (Eds.), GeneReviews((R)).
Ori-McKenney, K.M., Vallee, R.B., 2011. Neuronal migration defects in the Loa dynein mutant mouse. Neural Dev. 6, 26. https://doi.org/10.1186/1749-8104-6-26. May 25.
Pan, Y.H., Wu, N., Yuan, X.B., 2019. Toward a better understanding of neuronal migration deficits in autism Spectrum disorders. Front. Cell Dev. Biol. 7, 205. https://doi.org/10.3389/fcell.2019.00205.
Pfister, K.K., Shah, P.R., Hummerich, H., et al., 2006. Genetic analysis of the cytoplasmic dynein subunit families. PLoS Genet. 2 (1) https://doi.org/10.1371/journal.pgen.0020001. Jan. e1.
Pilling, A.D., Horiuchi, D., Lively, C.M., Saxton, W.M., 2006. Kinesin-1 and dynein are the primary motors for fast transport of mitochondria in Drosophila motor axons. Mol. Biol. Cell 17 (4), 2057–2068. https://doi.org/10.1091/mbc.e05-06-0526. Apr.
Poirier, K., Lebrun, N., Broix, L., et al., 2013. Mutations in TUBG1, DYNC1H1, KIF5C and KIF2A cause malformations of cortical development and microcephaly. Nat. Genet. 45 (6), 639–647. https://doi.org/10.1038/ng.2613. Jun.
Qiu, R., Zhang, J., Xiang, X., 2019. LIS1 regulates cargo-adapter-mediated activation of dynein by overcoming its autoinhibition in vivo. J. Cell Biol. 218 (11), 3630–3646. https://doi.org/10.1083/jcb.201905178. Nov 4.
Rakic, P., 2003. Elusive radial glial cells: historical and evolutionary perspective. Glia 43 (1), 19–32. https://doi.org/10.1002/glia.10244. Jul.
Ray, A.K., DuBois, J.C., Gruber, R.C., et al., 2017. Loss of Gas6 and Axl signaling results in extensive axonal damage, motor deficits, prolonged neuroinflammation, and less remyelination following cuprizone exposure. Glia. https://doi.org/10.1002/glia.23214. Sep 19.
Reck-Peterson, S.L., Redwine, W.B., Vale, R.D., Carter, A.P., 2018. The cytoplasmic dynein transport machinery and its many cargoes. Nat. Rev. Mol. Cell Biol. 19 (6), 382–398. https://doi.org/10.1038/s41580-018-0004-3. Jun.
Reimer, J.M., DeSantis, M.E., Reck-Peterson, S.L., Leschziner, A.E., 2023. Structures of human dynein in complex with the lissencephaly 1 protein, LIS1. Elife 12. https://doi.org/10.7554/eLife.84302. Jan 24.
Roberts, A.J., Kon, T., Knight, P.J., Sutoh, K., Burgess, S.A., 2013. Functions and mechanics of dynein motor proteins. Nat. Rev. Mol. Cell Biol. 14 (11), 713–726. https://doi.org/10.1038/nrm3667. Nov.
Romero, D.M., Zaidi, D., Cifuentes-Diaz, C., et al., 2023. A human dynein heavy chain mutation impacts cortical progenitor cells causing developmental defects, reduced brain size and altered brain architecture. Neurobiol. Dis. 180, 106085. https://doi.org/10.1016/j.nbd.2023.106085. May.
Roossien, D.H., Miller, K.E., Gallo, G., 2015. Ciliobrevins as tools for studying dynein motor function. Front. Cell. Neurosci. 9, 252. https://doi.org/10.3389/fncel.2015.00252.
Schiavo, G., Greensmith, L., Hafezparast, M., Fisher, E.M., 2013. Cytoplasmic dynein heavy chain: the servant of many masters. Trends Neurosci. 36 (11), 641–651. https://doi.org/10.1016/j.tins.2013.08.001. Nov.
Schroer, T.A., 2004. Dynactin. Annu. Rev. Cell Dev. Biol. 20, 759–779. https://doi.org/10.1146/annurev.cellbio.20.012103.094623.
Tsai, J.W., Bremner, K.H., Vallee, R.B., 2007. Dual subcellular roles for LIS1 and dynein in radial neuronal migration in live brain tissue. Nat. Neurosci. 10 (8), 970–979. https://doi.org/10.1038/nn1934. Aug.
Tynan, S.H., Gee, M.A., Vallee, R.B., 2000. Distinct but overlapping sites within the cytoplasmic dynein heavy chain for dimerization and for intermediate chain and light intermediate chain binding. J. Biol. Chem. 275 (42), 32769–32774. https://doi.org/10.1074/jbc.M001537200. Oct 20.
Vallee, R.B., Tai, C., Faulkner, N.E., 2001. LIS1: cellular function of a disease-causing gene. Trends Cell Biol. 11 (4), 155–160. https://doi.org/10.1016/s0962-8924(01)01956-0. Apr.
Vissers, L.E., de Ligt, J., Gilissen, C., et al., 2010. A de novo paradigm for mental retardation. Nat. Genet. 42 (12), 1109–1112. https://doi.org/10.1038/ng.712. Dec.
Walker, J.E., Saraste, M., Runswick, M.J., Gay, N.J., 1982. Distantly related sequences in the alpha- and beta-subunits of ATP synthase, myosin, kinases and other ATP-requiring enzymes and a common nucleotide binding fold. EMBO J. 1 (8), 945–951. https://doi.org/10.1002/j.1460-2075.1982.tb01276.x.
Weedon, M.N., Hastings, R., Caswell, R., et al., 2011. Exome sequencing identifies a DYNC1H1 mutation in a large pedigree with dominant axonal Charcot-Marie-tooth disease. Am. J. Hum. Genet. 89 (2), 308–312. https://doi.org/10.1016/j.ajhg.2011.07.002. Aug 12.
Willemsen, M.H., Vissers, L.E., Willemsen, M.A., et al., 2012. Mutations in DYNC1H1 cause severe intellectual disability with neuronal migration defects. J. Med. Genet. 49 (3), 179–183. https://doi.org/10.1136/jmedgenet-2011-100542. Mar.
Yang, H., Wang, H., Shivalila, C.S., Cheng, A.W., Shi, L., Jaenisch, R., 2013. One-step generation of mice carrying reporter and conditional alleles by CRISPR/Cas-mediated genome engineering. Cell 154 (6), 1370–1379. https://doi.org/10.1016/j.cell.2013.08.022. Sep 12.
Yang, M.L., Shin, J., Kearns, C.A., et al., 2015. CNS myelination requires cytoplasmic dynein function. Dev. Dyn. 244 (2), 134–145. https://doi.org/10.1002/dvdy.24238. Feb.
Yonemura, Y., Sakai, Y., Nakata, R., Hagita-Tatsumoto, A., Miyasaka, T., Misonou, H., 2023. Active transport by cytoplasmic dynein maintains the localization of MAP2 in developing neurons. bioRxiv. https://doi.org/10.1101/2023.04.26.538370. Apr 30.
Zhu, J.W., Li, Y.F., Wang, Z.T., Jia, W.Q., Xu, R.X., 2016. Toll-like receptor 4 deficiency impairs motor coordination. Front. Neurosci. 10, 33. https://doi.org/10.3389/fnins.2016.00033.